DOE AWARD NUMBER: DE-SC0006713

FINAL REPORT

Project Title: Improving the Representation of Soluble Iron in Climate Models

Recipient and PD/PI: Carlos Perez Garcia-Pando, Columbia University

Other team Members:
Jan P. PERLWITZ
Ron L. MILLER

March 13, 2016

1 Executive Summary

Mineral dust produced in the arid and semi-arid regions of the world is the dominant source of iron (Fe) in atmospheric aerosol inputs to the open ocean. The bioavailable Fe fraction of atmospheric dust is thought to regulate and occasionally limit the primary productivity in large oceanic regions, which influences the CO2 uptake from the atmosphere affecting the Earth's climate. Because Fe bioavailability cannot be directly measured, it is assumed that the dissolved Fe or highly reactive Fe in the dust is bioavailable. The fraction of soluble Fe in dust is mainly controlled by:

(1) the mineral composition of the soils and the emitted dust from the source areas;
(2) the atmospheric processing that converts the Fe in Fe-bearing minerals into highly soluble forms of Fe.

The project has mainly focused on constraining the mineral composition of dust aerosols (1), a previously neglected, yet a key issue to constrain the deposition of soluble iron. Deriving aerosol mineral composition requires global knowledge of the soil mineral content, which is available from poorly constrained global atlases. In addition, the mineral content of the emitted aerosol differs from that of the parent soil. Measurements of soil mineral fractions are based upon wet sedimentation (or 'wet sieving') techniques that disturb the soil sample, breaking aggregates that are found in the original, undispersed soil that is subject to wind erosion. Wet sieving alters the soil size distribution, replacing aggregates that are potentially mobilized as aerosols with a collection of smaller particles. A major challenge is to derive the size-distributed mineral fractions of the emitted dust based upon their fractions measured from wet-sieved soils. Finally, representations of dust mineral composition need to account for mixtures of minerals. Examination of individual particles shows that iron, an element that is central to many climate processes, is often found as trace impurities of iron oxide attached to aggregates of other minerals. This is another challenge that has been tackled by the project.

The project has produced a major step forward on our understanding of the key processes needed to predict the mineral composition of dust aerosols by connecting theory, modeling and observations. The project has produced novel semi-empirical and theoretical methods to estimate the emitted size distribution and mineral composition of dust aerosols. These methods account for soil aggregates that are potentially emitted from the original undisturbed soil but are destroyed during wet sieving. The methods construct the emitted size distribution of individual minerals building upon brittle fragmentation theory, reconstructions of wet-sieved soil mineral size distributions, and/or characteristic mineral size distributions estimated from observations at times of high concentration. Based on an unprecedented evaluation with a new global compilation of observations produced with the project support, we showed that the new methods remedy some key deficiencies compared to the previous state-of-the-art. This includes the correct representation of Fe-bearing phyllosilicates at silt sizes, where they are abundant according to observations. In addition, the quartz fraction of silt particles is in better agreement with measured values. In addition, we represent an additional class of iron oxide aerosol that is a small impurity embedded within other minerals, allowing it to travel farther than in its pure crystalline state. We assume that these impurities are least frequent in soils rich in iron oxides (as a result of the assumed effect of weathering that creates pure iron oxide crystals).

The mineral composition of dust is also important to other interaction with climate - through shortwave absorption and radiative forcing, nucleation of cloud droplets and ice crystals, and the heterogeneous formation of sulfates and nitrates - and to its impacts upon human health. Despite the importance of mineral composition, models have typically assumed that soil dust aerosols have globally uniform composition. The results of this project will allow an improved estimation of the dust effects upon climate and health.

2 Comparison of the actual accomplishments with the goals and objectives of the project

The original goals of the project were to develop atmospheric iron lifecycle module for an Earth System model (GISS ModelE); evaluate and constrain the model for dust and total and soluble iron with a worldwide set of observations, including multi-year measurements of daily dust and iron concentration at Izaña Observatory, downwind of the Sahara; calculate regional variations in the soluble iron deposition, and advance in our understanding of the relative role of the different mechanisms involved in the atmospheric processing of iron. A key aspect of the proposal was to explicitly take into account the mineral composition of dust, which was disregarded in previous studies.

The accomplishments of the proposal include the improved representation of the lifecycle of dust minerals based on the development of novel methodologies; the evaluation and constraining of the model for dust, minerals and total iron based on an unprecedented compilation of observations produced within the project, and multi-year measurements of daily dust and iron concentration at Izaña Observatory; and the development of a soluble iron scheme for models that takes into account the mineral composition. One of the key assumptions of the proposal was that the available global atlases of soil mineral composition could be directly used to estimate the mineral composition of the emitted dust aerosols in the model. However, the first results showed a very poor skill of the model to reproduce the observed mineral fractions. Because the representation of the mineral composition is a requirement to constrain the deposition of soluble Fe we considered that it was critical to tailor this problem in detail. Therefore a large part of the proposal was devoted to this aspect which resulted in the development of the above-mentioned novel approaches.

3 Summary of project activities for the entire period of funding

3.1 Activity 1. Initial hypothesis and the identification of challenges to represent the mineralogical dust cycle model

Our goal is to predict regional variations of soluble iron deposition. The first requirement to achieve that goal is to be able to predict the dust mineral composition as a function of particle size. For comparison, ModelE2 previously predicted (and most models currently do) the size distribution of dust aerosols, but assuming a globally uniform mineral content. Regional variations in soil mineral

composition lead to variations in dust aerosol composition.

Claquin et al. (1999) proposed that soil mineral content is related to the soil type provided by a soil map. The relation between soil type and fractional mineral abundance within the clay and silt-size categories is summarized in the Mean Mineralogical Table (MMT). Estimating the soil mineral composition additionally requires information about the fraction of clay and silt-sized particles present at each location, available from global databases of soil texture.

During the first year we detected major challenges to simulate the global mineral composition that were overlooked in previous studies. First, the relation between mineral composition and soil type is derived from a limited number of measurements that are particularly scarce in the arid and semi-arid areas that contain dust sources. This relation assumes that regional variations in mineral content within a particular soil type can be neglected. Second, measurements are based on wet sedimentation ('wet sieving') techniques that disturb the soil samples, breaking the aggregates that are found in the original, undispersed soil that is subject to wind erosion. Wet sieving alters the soil size distribution, replacing aggregates with a collection of smaller particles. Wet sieving is also used to characterize the soil texture in global data sets that give the fraction of clay, silt and sand-sized particles at each location. Third, representations of aerosol mineral composition need to account for mixtures of minerals. Examination of individual particles shows that iron is often found as trace impurities of iron oxide attached to aggregates of other minerals.

In the absence of knowledge, previous studies had assumed that the emitted size distribution of each mineral closely resembles that of the wet-sieved soil and did not consider iron oxide internal mixtures. This assumption represented our original working hypothesis to simulate the global distribution of dust mineral as a previous step to calculate regional variations in Fe and soluble Fe. After testing this assumption we determined that the original hypothesis had to be rejected. As described below, our project has shown that the differences in the mineral size distribution between wet-sieved soils and the emitted aerosol particles are critical.

Finally, model evaluation is challenged by limited global measurements of size-resolved aerosol composition. Many of the available measurements dispersed in the literature are from field campaigns or ship cruises of limited duration, while changes in the sampling and analysis methods through time contribute additional uncertainty.

3.2 Activity 2. Analysis of the problem

The next step was devoted to the analysis of these key challenges using observations and theoretical considerations. We identified that differences between the size distribution of the soil after wet sieving and during emission are potentially large. Figure 1 shows the volume distribution as a function of particle size for common airborne minerals at Tinfou, Morocco, during the Saharan Mineral Dust Experiment (SAMUM) campaign of 2006 (Kandler et al., 2009). Each particle consists of a single mineral or aggregates of different minerals. For example, images suggest that iron oxides are consistently present both in pure crystalline form and as small impurities attached to other minerals (Scheuvens and Kandler, 2014). Figure 1 distinguishes between conditions of high and

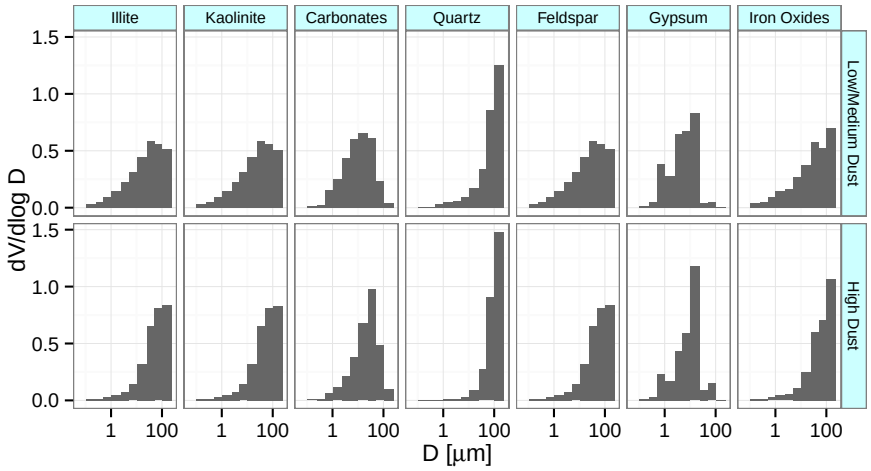

Figure 1: Volume distribution of minerals with respect to particle diameter, calculated as described in the Supplement, using size-resolved dust number and volume fraction measured by Kandler et al. (2009). The size bins correspond to the following range of particle diameter (μm): 0.1–0.25; 0.25–0.5; 0.5–1.0; 1.0–2.5; 2.5–5.0; 5.0–10.0; 10.0–25.0; 25.0–50.0; 50.0–100.0.; 100.0–250.0. Upper panel: low/medium dust concentration; lower panel: high dust concentration. The size distribution is normalized so that the total volume is unity for each mineral.

low aerosol concentration. The presence of larger particles at times of high concentration (Fig. 1, bottom row) suggests that this size distribution is a better indicator of the emitted size distribution. Figure 1 shows that the mass of phyllosilicate aerosols like illite and kaolinite is predominantly within silt particle sizes. That is, phyllosilicate aerosols that are nominally 'clay' minerals are also observed at larger silt sizes. This is corroborated by aerosol measurements at other locations where clay aggregates routinely exceed 2 μm in particle diameter. Wet sieving breaks up these larger particles, and models that do not account for this potentially allow a significant fraction of phyllosilicates to travel unrealistically far from their source as a result of insufficient gravitational deposition. This has implications for the delivery of phyllosilicate iron to fertilize photosynthesis within distant marine ecosystems. The presence of significant clay mass at silt diameters suggested that aggregates in the original soil subject to wind erosion are significantly dispersed by wet sieving. An important challenge was thus to calculate the emitted size distribution of each mineral, given that information is only available about the fully dispersed soil.

Direct entrainment by the wind of the smaller soil particles that travel thousands of kilometers downwind from their source (whose diameters are generally below 20 μm) is hindered by the cohesive force that binds adjacent particles. Larger soil grains or aggregates are more easily lifted because this cohesion can be overcome by the wind stress acting over a larger area. Most of the smaller particles that are transported globally are entrained into the atmosphere during the fragmentation of aggregates that are bombarded by larger particles, or else are large enough to be lifted directly by the wind and disintegrated through repeated collisions. Fragmentation is an important source of clay-sized aerosols, although the abundance of phyllosilicate mass at silt sizes in Fig. 1

made it clear that many soil aggregates are not completely disintegrated into clay-sized aerosols during mobilization.

An additional modeling challenge is that different minerals may have different size distributions in the soil and may not be equally susceptible to disaggregation and fragmentation during wet sieving and emission, respectively. The size distribution of each mineral in Fig. 1 allows the comparison of the characteristic particle size between different minerals. For example, Fig. 1 shows that a greater fraction of quartz mass is found at large particle sizes, compared to other minerals. Differences in the aerosol size distribution among minerals may result from contrasting size distributions in the parent soil as well as different aggregation and fragmentation properties of each mineral. A model must therefore account for these contrasts to reproduce observations that far-travelled aerosols are depleted in quartz compared to the fraction of this mineral in the parent soil.

The rate of aerosol removal is distinguished in part by particle density that controls the speed of gravitational settling. Many minerals commonly observed to comprise dust particles have similar densities, suggesting that external mixing is a reasonable idealization that is attractive for its computational simplicity. However, iron oxides like hematite and goethite have densities that are twice that of the other minerals, and would thus be removed by gravitational settling within roughly half the distance from their source. This density contrast means that mineral combinations containing iron oxides cannot be represented implicitly as external mixtures like combinations of other minerals. The first tests sowed that iron oxide mixtures must be treated explicitly as separate prognostic variables that are distinct from pure crystalline forms of this mineral. In general, impurities of iron oxides are only a small fraction of the total particle mass, and only slightly perturb the particle density that is determined primarily by the host mineral. Iron oxides present as a small impurity will travel farther than in their pure, crystalline form. This represented another key challenge.

3.3 Activity 3. Development of novel approaches

The transformation of the particle size distribution of the (undispersed) parent soil into the emitted size distribution is a complicated process that depends upon wind speed and the physical properties of the soil and land surface. However, measurements suggest that for the smallest particles that are transported globally, the emitted size distribution is approximately independent of wind speed and soil properties. The theory of brittle fragmentation has been invoked to suggest that this invariance is robust, despite limited measurements of size-resolved emission (Kok, 2011). In arid soils, mineral aggregates are typically most abundant at diameters between a few tens and a few hundred microns, according to measurements that minimally disturb the aggregates. Brittle fragmentation theory proposes that energetic and repeated collisions, in this case between soil aggregates mobilized by saltation, will result in emitted aggregate diameters that are mostly smaller than a scale λ. According to this theory, the number concentration N of emitted particles varies inversely with the square of the diameter D:

$$\frac{dN}{d\ln D} \propto \frac{1}{D^2} \exp\left[-\left(\frac{D}{\lambda}\right)^3\right] \text{ for } D > x_0, \tag{1}$$

where the exponential imposes an upper bound on the emitted size range near diameter λ. The inverse-square dependence in (1) remains valid for diameters as small as x_0, the "indivisible" scale, where the material properties of the individual particles comprising the aggregates resist further disintegration.

For soil aggregates, Kok (2011) proposes that there is a range of indivisible scales that is given by the distribution of soil particle diameters D_s after wet sieving, when aggregates have been dispersed and further disintegration is difficult. Then, if $p(D_s)\,dD_s$ is the distribution of wet-sieved diameters, the emitted number concentration is given by:

$$\frac{dN}{d\ln D} = \frac{1}{c_N D^2} \exp\left[-\left(\frac{D}{\lambda}\right)^3\right] \int_0^D p(D_s)\,dD_s \tag{2}$$

where c_N is a normalization factor. The effect of the integral in (2) is to reduce the number concentration at smaller aggregate diameters compared to the inverse-square power law given by (1). This reduction occurs because emitted aggregates of diameter D can be comprised only of particles with smaller indivisible scales (given by D_s). Thus, the integral is the product of an inverse-square power-law dependence with the distribution of indivisible scales identified from the wet-sieved soil.

The emitted number concentration (2) derived from brittle fragmentation theory is independent of the size distribution of the original, undispersed soil that is subject to wind erosion. The approximate upper bound λ of emitted aggregates is estimated as $12 \pm 1\,\mu m$ by Kok (2011), who performed a least-squares fit to the few available measurements of the emitted size distribution, after estimating $p(D_s)\,dD_s$ from measured size distributions of dispersed arid soils. This value is roughly ten percent of a typical aggregate diameter in the original soil and bounds the diameters of a majority of the particles that are dispersed globally downwind of their source.

Eq. (2) predicts that the volume distribution of emitted aggregates is shifted toward larger diameters, compared to the distribution of the wet-sieved soil, consistent with the measurements shown in Fig. 1. This is illustrated by Fig. 2, where the normalized distribution of emitted volume is shown as a black line, derived from the corresponding distribution of the fully dispersed soil shown in orange. In this example, the ratio of clay-sized mass to silt is 0.5 in the fully dispersed soil but only 0.05 after brittle fragmentation and emission of the undispersed soil. (The silt fraction here represents the sum of particle diameters up to 20 μm, below which we assume Eq. 2 is applicable.) That is, brittle fragmentation of aggregates during saltation preserves a greater fraction of mass at silt sizes compared to the breaking of aggregates during dispersion of the soil prior to measurement.

The dotted curve in Fig. 2 shows the contribution to silt emission from particles with indivisible scales at clay sizes in the fully dispersed soil. This contribution corresponds to about 45 % of the emitted silt mass.

The process of brittle fragmentation that leads to the emitted size distribution in Fig. 2 creates particles with diameters extending up to approximately λ. We assumed that the specific range of validity is below 20 μm. At larger diameters, the emitted size distribution evolves through saltation

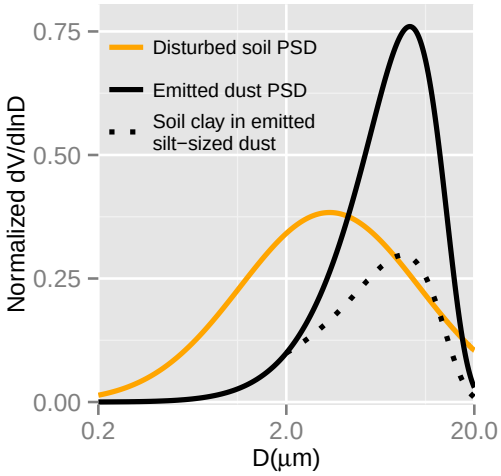

Figure 2: Size distribution of emitted dust (black line) derived from Eq. (2) with $\lambda = 12\mu m$ (Kok, 2011). The orange curve describes the arid dispersed soil used in the calculation of $U(D)$ in Eq. (2), and is represented by a monomodal log-normal distribution with a volume median diameter of $3.4\mu m$ and geometric SD of 3.0. Both curves are and normalized over the range 0–$20\mu m$. The dotted line represents the contribution of dispersed soil clay particles to silt-sized dust aggregates calculated with Eq. (2) and in this example contributes 45 % of the emitted silt.

and sandblasting with a complicated dependence upon wind speed and soil properties (Kok, 2011). The range of emission by brittle fragmentation is mismatched with respect to the MMT whose silt size category extends to particle diameters up to 50 μm. To calculate the emitted fraction of clay and silt-sized particles over the size range corresponding to the MMT, we need to know the emitted size distribution between 20 and 50 μm.

Based on this theoretical and observational analysis we developed novel semi-empirical and theoretical methods to estimate the emitted size distribution and mineral composition of dust aerosols. The methods (briefly described below and detailed mathematically in Section 5 of this report) account for soil aggregates that are potentially emitted from the original undisturbed soil but are destroyed during wet sieving. The methods construct the emitted size distribution of individual minerals building upon brittle fragmentation theory, reconstructions of wet-sieved soil mineral size distributions, and/or characteristic mineral size distributions estimated from observations at times of high concentration.

3.3.1 Activity 3.1 Development of a semi-empirical approach combining theory and observations

Baseline/Original hypothesis

The baseline or original hypothesis assumes that the emitted mineral fractions are identical to those of the wet-sieved parent soil, which we referred to as the Soil Mineral Fraction (SMF) method. The

soil (and thus the emitted) mineral fractions are calculated by combining the MMT with global atlases of arid soil type and soil texture.

The MMT provides the fractional abundance for eight minerals within the clay and silt-size ranges of the soil as a function of arid soil type. For the clay-size range (whose diameters are less than 2μm), the MMT gives the fraction of phyllosilicates (illite, kaolinite, and smectite) along with quartz and calcite. Similarly, at silt sizes (with diameters between 2 and 50μm), the MMT gives the fraction of quartz and calcite along with feldspar, gypsum and hematite. According to the MMT, hematite is present in the soil only at silt sizes. Aerosol measurements show this mineral to be present at both clay and silt sizes, so we extended the size range of emitted hematite to include clay sizes. Given the limited measurements of this mineral in soil samples, we assumed for simplicity that the hematite fraction at clay sizes in identical to the silt fraction provided by the MMT. We refer to hematite more generally as 'iron oxide'. Similarly, we refer to calcite more generally as carbonate'.

The mineral fractions provided by the MMT for each size category are combined with the mass fraction of each size category provided by the soil texture atlas. This gives the size-resolved mineral fractions of the wet-sieved soil at each location.

After emission, the minerals are transported within five size classes with diameters extending between 0.1 and 32 μm. Clay-sized particles are transported in a single bin by ModelE2. For silt particles, the MMT gives the emitted fraction of each mineral summed between 2 and 50μm. It remains to distribute this fraction over the four silt categories transported by the model. For each mineral, we allocated the emitted silt fraction to the model size categories using a normalized distribution derived from measurements of dust concentration at Tinfou, Morocco (Kandler et al., 2009). In the SMF method, this allocation uses a distribution that is identical for all minerals.

New semi-empirical approach

We refer to this approach as the Aerosol Mineral Fraction (AMF) method to emphasize the difference between the aerosol and soil mineral fractions (in contrast to the SMF where these fractions are assumed to be identical). This difference results because wet sieving is more destructive of aggregates of soil particles than mobilization of the original, undispersed soil, where many of the aerosols are comprised of aggregates that resist complete disintegration during emission.

The full mathematical formulation is provided in Sect. 5 of this report. He we provide a brief qualitative description of the approach.

Brittle fragmentation theory provides a physically based method for reconstructing the emitted size distribution from the distribution measured after wet sieving (Kok, 2011). The emitted silt fraction consists not only of silt particles present in the wet-sieved soil, but also aggregates that were broken during wet sieving into clay-sized fragments. In the AMF simulation, we reaggregate these fragments heuristically. For each mineral, the emitted silt fraction is comprised of silt particles in the wet-sieved soil augmented in proportion to the mineral's wet-sieved clay fraction. The degree of augmentation is prescribed through a proportionality constant γ. We set $\gamma = 2$ for

our reference AMF method, although we have not made much effort to find an optimal value of this parameter. Results with $\gamma = 0$ are have been explored to illustrate the physical origin of the size and regional distributions of minerals within the AMF method, and their contrast with respect to those of the SMF method. The only mineral that is not reaggregated in the AMF simulation is quartz, whose physical integrity is assumed to be large enough to prevent disintegration during wet sieving. One effect of reaggregation is to introduce clay minerals (illite, kaolinite and smectite) as aerosols at silt sizes. This introduction is consistent with observations and in contrast to the SMF method, where aerosols comprised of clay minerals are absent at silt sizes, as prescribed by the MMT.

To apportion the emitted silt fraction of the AMF method into the ModelE2 transport categories, we combined the size distribution derived from brittle fragmentation theory (that is valid for diameters below roughly 20 μm) with the empirical volume fraction derived for each mineral. We calculated this fraction for each mineral separately. One consequence is that quartz emission in the AMF method is shifted toward larger diameters, compared to the SMF method. This has the effect of reducing the quartz fraction in the AMF experiment, due to the higher gravitational settling speed of larger particles.

Finally, for the AMF method, we allow iron oxides to be emitted not only in their pure, crystalline form, but additionally as impurities mixed with other minerals (The mathematical formulation is also available in Section 5 of this report). These mixtures are important for transporting iron far from its source, because pure iron oxides are more dense and vulnerable to gravitational removal than most other minerals that contain small inclusions or accretions of iron oxides. We assumed that the partitioning of iron oxides into mixtures and pure crystalline forms depends upon the soil fraction of iron oxides compared to the other minerals (as given by the MMT, including our extension to clay sizes). Soils enriched in iron oxides are assumed to be highly weathered, with a greater abundance of the pure, crystalline form. This is a heuristic representation of the effects of soil weathering that is more speculative than the remainder of the AMF method, and subject to future revision.

Figure 3 displays the fraction of mass emitted at each ModelE2 size bin according to the SMF and AMF methods. To construct this figure, we calculated the distribution of the emitted fraction within each size bin. For each SMF size bin, emission varies according to the local soil texture. For the AMF method, the size distribution varies additionally due to reaggregation of certain clay-sized minerals dispersed in the wet-sieved soil. For clay-sized particles (Figure 3), the median SMF fractional emission is 0.325, which is large compared to the AMF clay-sized fraction of 0.013 that is prescribed and spatially uniform, based upon observations of the emitted size distribution and the normalized volume fractions at Tinfou that we assume are universal. At silt sizes, the median of the *sum* of the AMF emission is also spatially uniform by prescription. Thus, individual AMF bins at silt sizes exhibit smaller variability, compared to the SMF method, whose silt fraction varies with the local soil texture.

Contrasts between the methods are apparent in the emitted fractions of the individual minerals, shown in Fig. 4. Within each size bin, distributions are calculated as in Fig. 3. The SMF method emits clay-sized dust aerosols that are comprised mostly of phyllosilicates with median values of

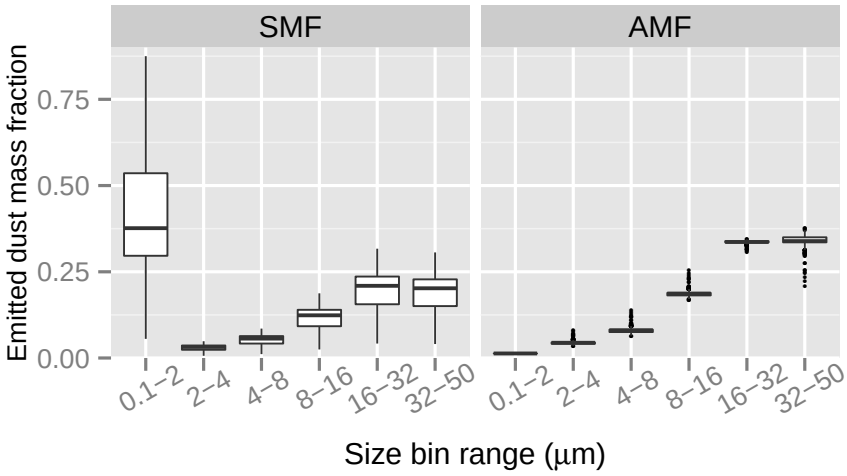

Figure 3: The distribution of the emitted dust mass fraction at each ModelE2 size bin for the soil mineral fraction (SMF) method (left) and the aerosol mineral fraction (AMF) method (right). Within each size bin, the box plots depicts the distribution with respect to the combinations of the 12 soil textures and the 28 arid soil types included in the MMT. For each combination, the sum over all sizes is one. At each bin, each combination within the distribution is weighted by the total emission (summed over all sizes) to emphasize prolific sources. Each box shows the range in which the central 50 % of the data fall. The box borders show the first and third quartiles and the crossbar shows the median. Outliers exceeding the quartile values by more than a factor of 1.5, the interquartile distance, are marked as points. Note that only diameters below 32 *mu*m are transported by the model.

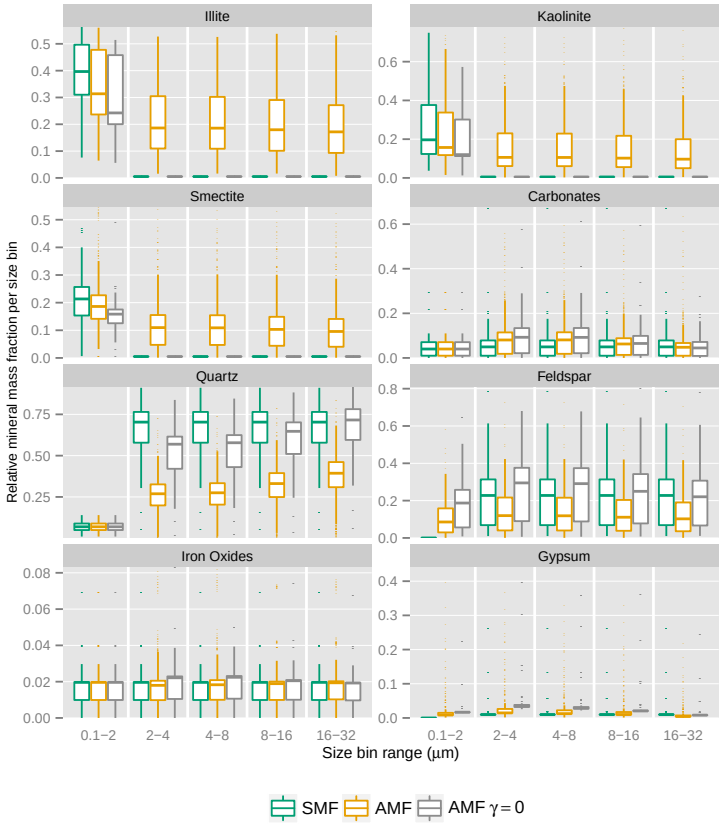

Figure 4: The distribution of the emitted mass fraction of each mineral at each ModelE2 size bin for the soil mineral fraction (SMF) method (green), the aerosol mineral fraction (AMF) method (orange), and the AMF method with $\gamma = 0$ (black). The box plots are constructed as in Fig. 3, but the emitted mineral fractions sum to unity within each *separate* size bin, to identify the mineral making the largest contribution to emission at that size.

0.40 for illite, 0.22 for smectite and 0.19 for kaolinite (Fig. 4, green). SMF phyllosilicates are absent among silt-sized aerosols, which are comprised mainly of quartz and feldspar, whose median values are 0.70 and 0.21, respectively. In the AMF, the mass fractions of clay-sized phyllosilicates are slightly reduced in comparison to the SMF, offset by increases of feldspar and gypsum (Fig. 4, orange). However, the AMF reintroduces phyllosilicate aggregates at silt sizes that are absent in the wet-sieved soil. This reintroduction is in proportion to γ, which is set equal to 2 in our reference AMF simulation. A consequence of this reintroduction is to substantially reduce the quartz and feldspar fractions in the silt size range (Fig. 4). Carbonate fractions at silt sizes are slightly increased compared to the SMF, particularly in the smallest silt-size model bins, due to the prescribed reaggregation of clay-sized soil particles. Figure 4 (black) displays the emitted mineral fractions for the AMF experiment, but without reaggregation of clay particles ($\gamma = 0$). The effect of $\gamma = 0$ is to preclude the reaggregation of clay soil particles that would otherwise be emitted at silt sizes.

3.3.2 Activity 3.2 Development of a purely theoretical approach: Extending brittle fragmentation theory

We also developed a purely theoretical approach by extending the explicit formulation of brittle fragmentation theory to individual minerals. The full formulation and description is provided in Sect. 5 of this report.

3.4 Activity 4. Compilation and analysis of observations

A major challenge was the availability of observations for model evaluation. Another important activity was the compilation measurements of mineral fractions of dust aerosols from almost sixty studies published between the 1960s and the present day that are available in Table S1 of the Supplement in Perlwitz et al. (2015b). We also analyzed the uncertainties in these observations and their evolution through time. Roughly one-third of the studies are in common with a recent compilation focusing on North African sources by Scheuvens et al. (2013). Our compilation includes measurements of dust concentration and deposition, both from land stations and ship cruises. A few studies provide measurements of dust deposited in permanent snow fields. Measurements are not equally distributed over all dust source regions, and mostly sample dust transported from North Africa, the Middle East and Asia (Fig. 5). Only two studies provide measurements downwind of southern African sources. No studies were found for dust from North America, while only one site is affected by the Australian dust plume. Generally, most of the measurements for aerosol mineral composition are in the Northern Hemisphere and there is underrepresentation of the Southern Hemisphere. Also, many of the measurements in earlier decades were confined to the relative proportions of phyllosilicates. Methods to determine the mineral composition of dust aerosols have varied over time, and the measurements in our compilation that are based on various instruments and analytical methods contain different biases and uncertainties. Systematic studies of the mineral composition of atmospheric soil dust started in the 1960s. The mineral composition of airborne dust was usually determined from samples collected on suspended nylon mesh over land or ships. Typically, the collection efficiency of the mesh was assumed to be 50%, but the true value depends upon particle size and wind velocity. Thus, mesh collection introduces a bias towards larger dust particles, and potentially overestimates the fraction of minerals such as quartz, whose abundance peaks at large particle sizes. Other studies analyzed dust deposited on ship decks.

Since the 1990s, airborne dust has been more commonly sampled with other instruments, like high-volume air samplers or low-volume air samplers. These samples extract dust from the air with polycarbonate or quartz microfibre filters, cellulose filters, or other filters. The finest aerosol particles can get trapped in the quartz fibre filters before the sample is treated for the mineral analysis, a source of collection inefficiency and uncertainty. The relative mass fractions of the collected minerals are often derived from X-ray diffraction (XRD) spectra. The wavelengths of spectral peaks give information about elemental and mineral composition, while the mass fraction relative to other minerals is determined by area under the peak. Characterization of the area (rather than the peak) increases the sensitivity to particle diameters less than 10 μm that cause peak broadening. XRD analysis is most effective for minerals with a regular crystal structure whose spectral peaks are well defined. However, certain minerals like phyllosilicates consist of varying amounts of amorphous material whose mass is difficult to quantify using XRD. Among the various minerals

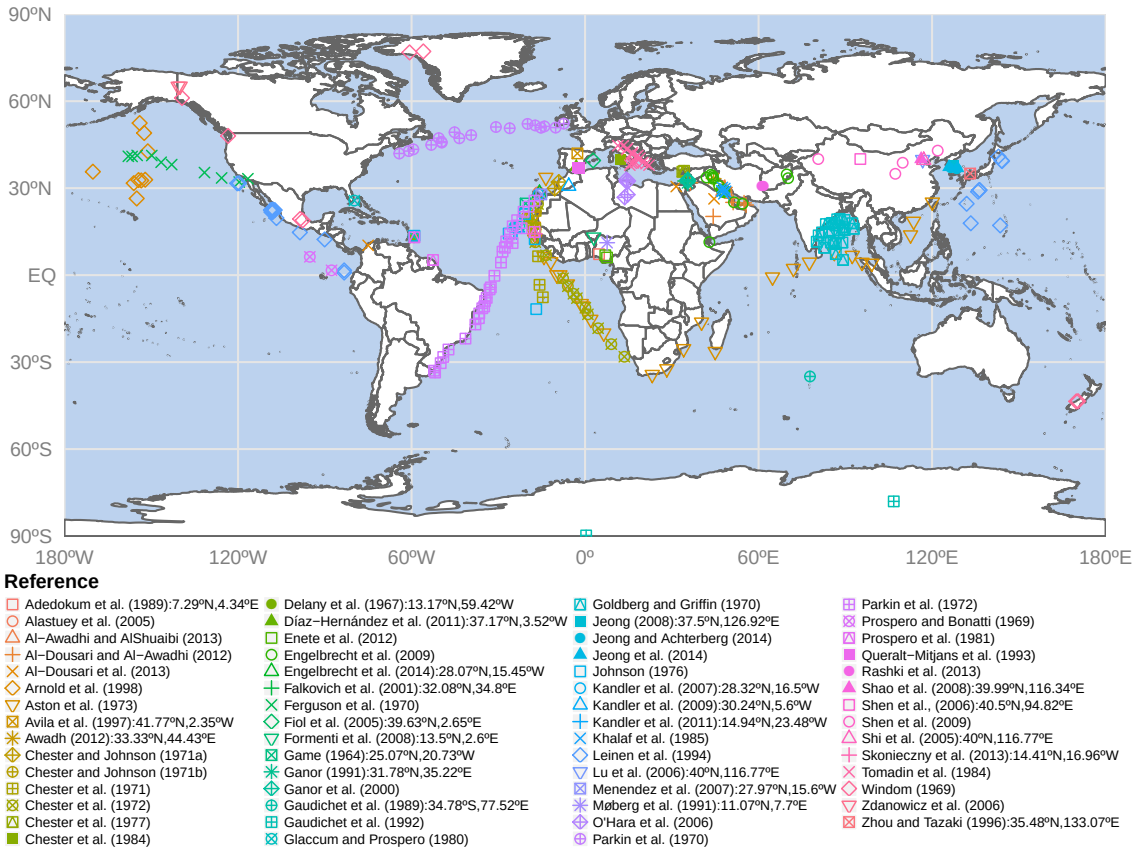

Figure 5: Locations of measured mineral fractions compiled from the literature used for the evaluation of the simulations. References with geographical coordinates in the legend provide measurements only for this single location; otherwise, references provide measurements for multiple locations.

considered, the fraction of smectite is one of the most difficult to estimate. Its spectral peaks are small and can lie within the noise level of the XRD analysis. This has been interpreted as the result of low concentration and poor crystallization. This is additionally due to the frequent interleaving of smectite with illite and other minerals like chlorite, both in soils and aerosols, which can lead to misidentification of the individual phyllosilicates. As a consequence, smectite is occasionally reported only in combination with illite.

The composition of airborne particles is increasingly studied by scanning electron microscope (SEM) images of individual particles along with statistical cluster analysis of elemental composition. Both XRD and SEM measurements are disproportionately sensitive to composition on the particle surface, which may include coatings resulting from chemical reactions with other species, compared to the particle interior. All the observations used for our evaluation are based on measurements of the mineral fractions of dust aerosols at the surface. A few studies also provide aircraft measurements. Those data are not taken into consideration but will be included in future evaluation of simulated vertical profiles. As prognostic models of mineral composition become more common, we hope that mineral identification within aerosol samples becomes more uniform and routine.

3.5 Activity 5. Development of an evaluation methodology for minerals

The challenge for model evaluation was the difference in record length between climate model output and the mineral observations. Deposition is measured over periods as short as a week. Measurements of surface concentration are based mostly on daily sampling, with reported values derived from a few days. In contrast, the output from model simulations consists of a continuous stream of data, from which typically monthly averages are calculated. The mineral fractions used for evaluation reflect the composition of the soil at the source region. These fractions are probably more consistent than the absolute concentration of the separate minerals used to form this ratio, at least in those remote regions where a single source dominates the supply. Thus, measurements of mineral fractions from a few days may be representative of the entire month. Closer to a source, the mineral fractions may be more variable, with episodic increases of quartz and other minerals that are abundant at large diameters during dust storms.

For each reference providing measurements, we calculated a time average that can be compared to the model output. In some cases, we estimated a monthly average using daily measurements that are available for only a subset of the month. Our simulations covered only the 9 years between 2002 and 2010, but some of the measurements date back to the 1960s. We assumed that multi-decadal variability in the mineral fractions of dust aerosols at individual locations is small compared to the fractions themselves. A thorough discussion of the sampling uncertainty is provided in Appendix A of Perwitz et al. (2015b).

The model simulates eight minerals. However, measurements may include additional minerals that are not simulated. Other measurements may not include all of the simulated minerals. To make the measured and simulated mineral fractions comparable, we recalculated the fractions at each individual data point using only minerals present in both the measurements and the model. We caution that this renormalization can be misleading if some minerals that contribute to the total

dust mass were simply not reported. (The mineral fraction measurements compiled in Table S1 of the Supplement in Perlwitz et al. (2015b) include all reported minerals, including both those simulated and those omitted from the ModelE2.)

To account for different size ranges of the model and measurements, we interpolated the mass fractions from the model size bins to the size range of the measurements. For measurements of total suspended particles (TSP), we compared to the sum over the entire model size range. Since this range extends only to 32 μm, this can lead to a positive bias in the observations for minerals like quartz that are more abundant at larger particle sizes, particularly at measurement locations near dust sources.

We compared the measured and simulated mineral fractions and ratios using scatterplots. We calculated the normalized bias (nBias) and normalized root mean squared error (nRMSE). Normalization was done by dividing the statistic by the average of the observed values used in each scatterplot. These summary statistics were computed without weighting: for example, with respect to the number of measurements used to compute the average value of each study. Such precision seems illusory given the incommensurate analytical uncertainty of different measurement types. Our goal was not to provide a detailed statistical analysis using these metrics, but to help identify robust improvement or deterioration of the new methods compared to the initial hypothesis.

The evaluation compared measurements from a specific location to the value at the corresponding grid box. In the case of ship cruises, we used the average along the cruise trajectory within each ocean, forming a model average with the corresponding sequence of grid boxes. Our comparison assumed that the grid size of the model is sufficient to resolve spatial variations of the measurements. This is not always the case, particularly near dust sources that are often geographically isolated, resulting in strong spatial contrasts of concentration.

3.6 Activity 6. Evaluation of experiments

Figures 6, 7, and 8 show the type of model evaluations performed. (We only show here results with the semi-empirical approach. The results with the purely theoretical approach are similar.) We show that the AMF method addresses key deficiencies of the SMF experiment in comparison to measurements. In particular, AMF phyllosilicates (that are nominally 'clay' minerals) are most abundant at silt sizes, while the silt fraction of quartz is reduced compared to the SMF value and in better agreement with measurements. In spite of the unrealistic behavior of the SMF method at silt sizes, both experiments show reasonable agreement with measurements when the mineral fractions are summed over the entire size range. This is because the emitted clay fraction in the SMF experiment is large relative to the AMF experiment. This extra emission of clay-sized phyllosilicates in the SMF simulation compensates for the absence of these minerals at silt sizes. Similarly, the reduced fraction of emission at silt sizes in the SMF experiment compensates for its excessive quartz fraction. The fractional emission of clay and silt sizes in the SMF experiment is based upon the local soil texture that is derived from measurements of the fully dispersed, wet-sieved soil. However, the large fraction of emitted clay-sized particles in the SMF method is inconsistent with emission measurements that show a relatively small and regionally invariant emitted clay fraction. Thus, measurements of mineral fractions that sum over all sizes do not distinguish between the AMF and

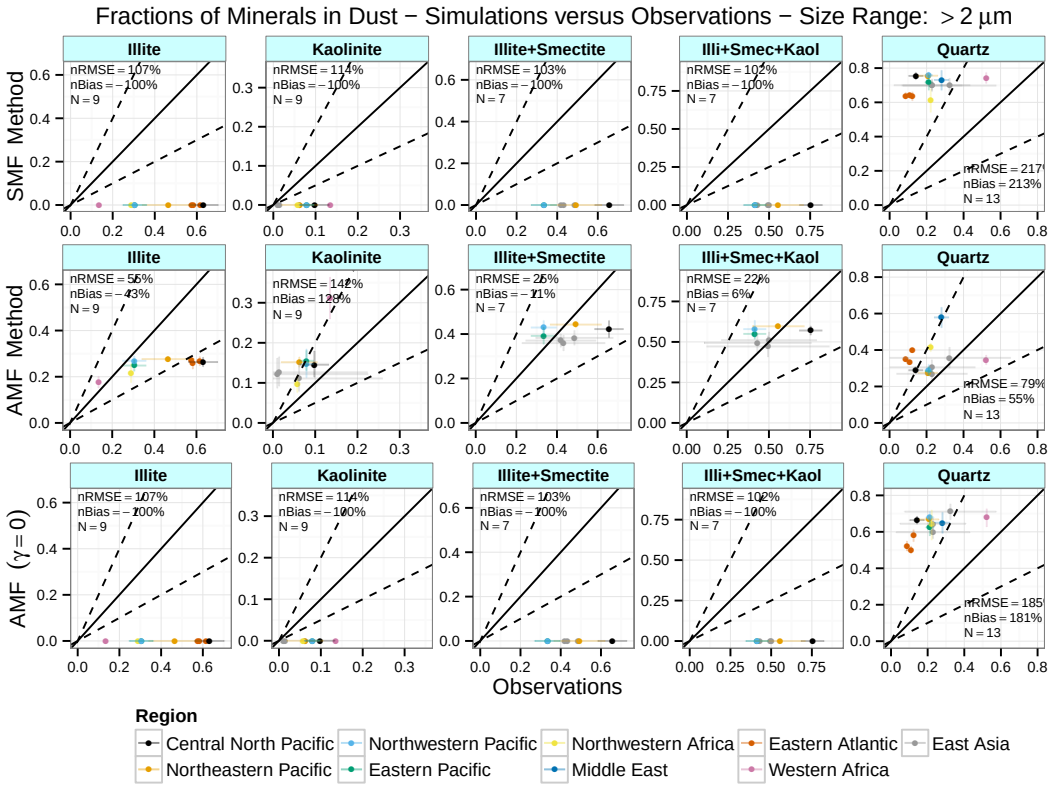

Figure 6: Scatter plot of mineral fractions of illite, kaolinite, the sum of illite and smectite, all phyllosilicates and quartz for silt particles (whose diameters are greater than 2 μm) simulated by the SMF, AMF and AMF ($\gamma = 0$) experiments vs. measurements. The dashed lines mark ratios of 2 : 1 and 1 : 2 between the simulated and observed mineral fractions. The horizontal and vertical error bars show the 95 % confidence interval.

SMF methods because of compensating errors in the latter that are more clearly distinguished by measurements limited to silt diameters. This is shown by a variation of the AMF experiment with reaggregation omitted ($\gamma = 0$), where silt-sized phyllosilicates are absent andthe mineral fractions compared poorly to bulk measurements.

We have also used the decadal record of dust concentration and elemental composition at the Izana Observatory to test our model (Fig. 9). We show that by restoring silt-sized aggregates of phyllosilicate soil particles, the AMF method better reproduces the size-resolved concentration measured at fine, coarse and super-coarse modes, while explaining the relatively invariant percent abundance of Fe and Al across size modes at IZO. Our attribution of the improvement of Fe to reaggregation is possible, because our model distinguishes between structural Fe in clays (that are reaggregated) and free-Fe found in iron oxides. In contrast, the SMF method that neglects reaggregation reproduces only the total (size-integrated) concentration, and only because of compensation of the underestimated silt mass by excessive clay-sized particles.

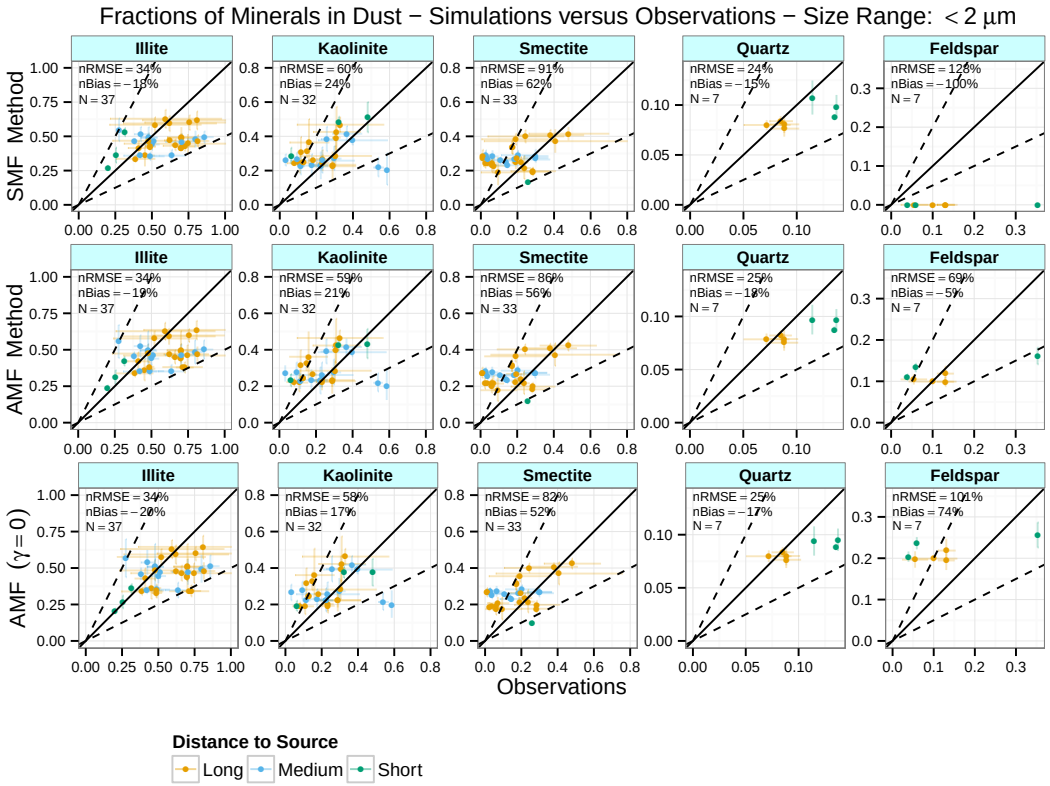

Figure 7: Same as Fig. 6 but for illite, kaolinite, smectite, quartz, and feldspar at clay diameters (less than 2 μm).

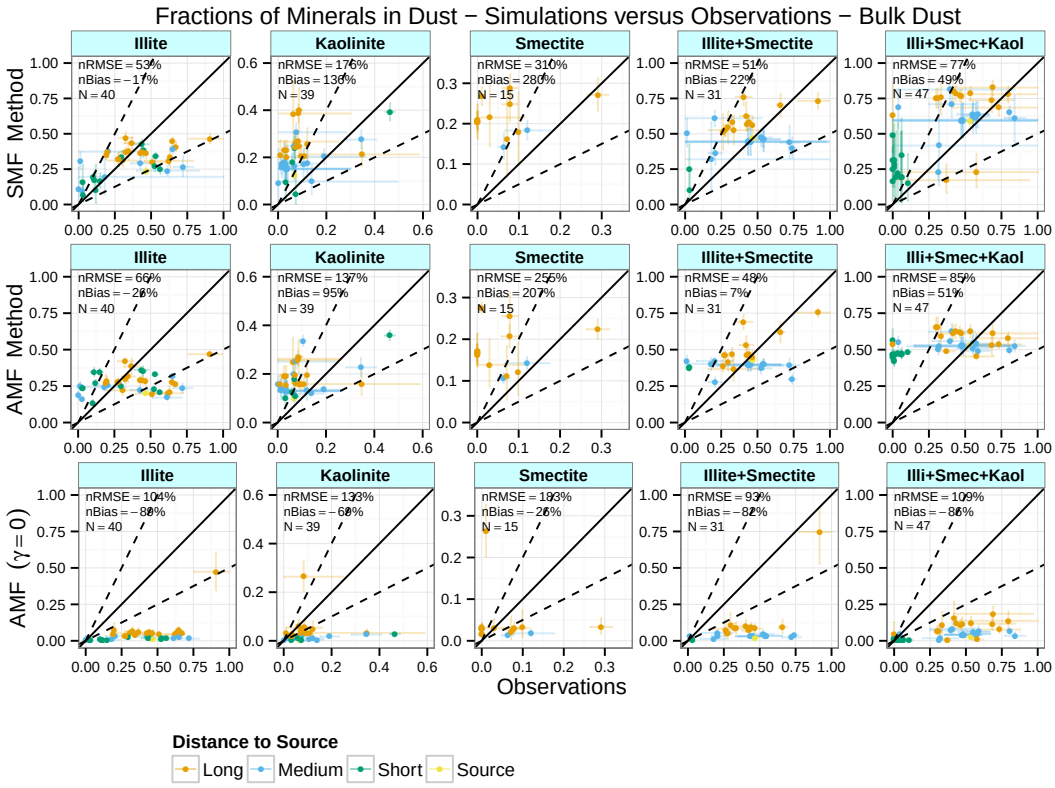

Figure 8: Same as Fig. 6 but for bulk (clay plus silt) mineral fractions of illite, kaolinite, smectite, the sum of illite and smectite, and all phyllosilicates.

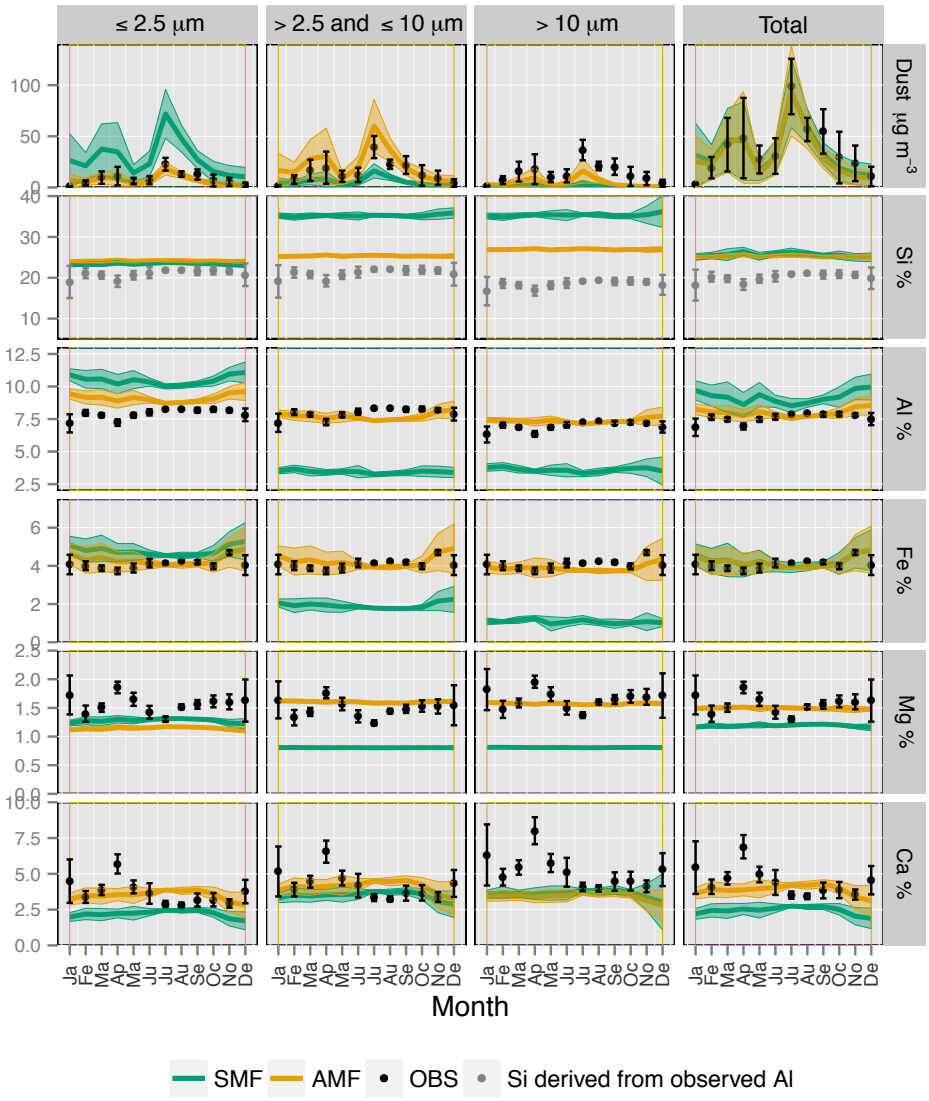

Figure 9: Comparison of the simulated annual cycle with measurements of dust concentration and percent abundances of Si, Al, Fe, Mg and Ca in fine, coarse, super-coarse modes and TSP at IZO. Green (yellow) lines and shaded contours represent the monthly means and two times the interannual monthly standard deviation with the SMF (AMF) experiment. Measurements are denoted as black dots, whose errors bars are the standard errors of the monthly means. The Si percent abundances were estimated from the measured Al abundances and are therefore displayed in grey. The model results are corrected by including an estimated average contribution of Fe-bearing minerals vermiculite, chlorite and goethite that are missing in the Mean Mineralogical Table of Claquin et al. (1999)

3.7 Activity 7. Soluble iron scheme

A scheme for Fe dissolution due to atmospheric chemical has been developed taking explicitly into account the pH, the mineral composition of iron-containing soils, the reactivity of iron species, the ambient temperature, and the degree of solution saturation. We have followed Ito and Xu (2014). We have tested and constrained a 1D box model with lab observations by Shi et al. (2011). Currently we are implementing and testing the scheme within GISS ModelE using the novel methods to contain the mineral global distribution.

3.8 Activity 8. Other

We started investigating the role of mineral types for ice nucleation for the development of ice nucleation parameterizations in a two-moment cloud microphysics scheme that is used in global models. Using the active site parameterization according to Aktinson et al. (2013), the concentration of ice forming nuclei (IFN) were then calculated offline. Sensitivity simulations were carried out with ModelE for different assumption of the mineral composition and size distribution. First results reveal that the proper representation of the volume size distribution of dust minerals is relevant for ice nucleation.

4 Products developed under the awards and technology transfer activities

4.1 Publications/conferences

4.1.1 Peer reviewed publications

1. Perlwitz, J. P.*, C. Perez Garcia-Pando*, and R. L. Miller*, 2015: Predicting the mineral composition of dust aerosols - Part 1: Representing key processes. Atmos. Chem. Phys., 15, 11593-11627, doi:10.5194/acp-15-11593-2015. (*Equal contribution)

2. Perlwitz, J. P., C. Perez Garcia-Pando, and R.L. Miller, 2015: Predicting the mineral composition of dust aerosols - Part 2: Model evaluation and identification of key processes with observations. Atmos. Chem. Phys., 15, 11629-11652, doi:10.5194/acp-15-11629-2015.

3. Miller, R.L., G.A. Schmidt, L.S. Nazarenko, N. Tausnev, S.E. Bauer, A.D. Del Genio, M. Kelley, K.K. Lo, R. Ruedy, D.T. Shindell, I. Aleinov, M. Bauer, R. Bleck, V. Canuto, Y.-H. Chen, Y. Cheng, T.L. Clune, G. Faluvegi, J.E. Hansen, R.J. Healy, N.Y. Kiang, D. Koch, A.A. Lacis, A.N. LeGrande, J. Lerner, S. Menon, V. Oinas, C. Perez Garcia-Pando, J.P. Perlwitz, M.J. Puma, D. Rind, A. Romanou, G.L. Russell, M. Sato, S. Sun, K. Tsigaridis, N. Unger, A. Voulgarakis, M.-S. Yao, and J. Zhang, 2014: CMIP5 historical simulations (1850-2012) with GISS ModelE2. J. Adv. Model. Earth Syst., 6, no. 2, 441-477, doi:10.1002/2013MS000266.

4. Perez Garcia-Pando, C., M. Stanton, P. Diggle, S. Trzaska, R.L. Miller, J.P. Perlwitz, J.M. Baldasano, E. Cuevas, P. Ceccato, P. Yaka, and M. Thomson, 2014: Soil dust aerosols and wind

as predictors of seasonal meningitis incidence in Niger. Environ. Health Perspect., 122, no. 7, 679-686, doi:10.1289/ehp.1306640.

5. Hickman, J.E., R.J. Scholes, T.S. Rosenstock, C. Perez Garcia-Pando, and J. Nyamangara, 2014: Assessing non-CO2 climate-forcing emissions and mitigation in sub-Saharan Africa. Curr. Opin. Environ. Sustain., 9-10, 65-72, doi:10.1016/j.cosust.2014.07.010.

6. Schulz, M., J.M. Prospero, A.R. Baker, F. Dentener, L. Ickes, P.S. Liss, N.M. Mahowald, S. Nickovic, C. Perez, S. Rodrguez, M. Manmohan Sarin, I. Tegen, and R.A. Duce, 2012: The atmospheric transport and deposition of mineral dust to the ocean: Implications for research needs. Environ. Sci. Technol., 46, 10390-10404, doi:10.1021/es300073u.

4.1.2 Under Peer Review

1. Perez Garcia-Pando, C., R.L. Miller, J.P. Perlwitz, S. Rodriguez, J. Prospero. Predicting the mineral composition of dust aerosols: Insights from elemental composition measurements at the Izaa Observatory. Geophysical Reseach Letters.

4.1.3 In preparation

1. Perez Garcia-Pando, C., R. L. Miller, J. P. Perlwitz, J. Kok. A theoretical approach to simulate the emission of soil dust aggregated minerals (Geophys. Rev).

4.1.4 Book Chapters

1. Miller, R.L., P. Knippertz, C. Perez Garcia-Pando, J.P. Perlwitz, and I. Tegen, 2014: Impact of dust radiative forcing upon climate. In Mineral Dust: A Key Player in the Earth System. P. Knippertz, and J.-B.W. Stuut, Eds. Springer, 327-357, doi:10.1007/978-94-017-8978-3˙13.

2. Benedetti, A., J.M. Baldasano, S. Basart, F. Benincasa, O. Boucher, M.E. Brooks, J.-P. Chen, P.R. Colarco, S. Gong, N. Huneeus, L. Jones, S. Lu, L. Menut, J.-J. Morcrette, J. Mulcahy, S. Nickovic, C. Perez Garcia-Pando, J.S. Reid, T.T. Sekiyama, T.Y. Tanaka, E. Terradellas, D.L. Westphal, X.-Y. Zhang, and C.-H. Zhou, 2014: Operational dust prediction. In Mineral Dust: A Key Player in the Earth System. P. Knippertz, and J.-B.W. Stuut, Eds. Springer, 223-265, doi:10.1007/978-94-017-8978-3˙10.

4.1.5 Invited conferences/workshops

1. Perez Garcia-Pando, C., R.L. Miller, J.P. Perlwitz, and P. Ginoux, 2016. Modeling Mineral Dust and its Effects upon Climate: Current Status and Challenges. 1st national french dust workshop (Organized by Paola Formenti). Paris, France. February 29, 2016.

2. Perlwitz, J.P., A.M. Fridlind, D.A. Knopf, C. Perez Garcia-Pando, and R.L. Miller, 2016: Dust Mineralogy and Ice Nucleation. Invited talk at King Abdullah University of Science and Technology, Thuwal, Saudi Arabia, February 18,2016.

3. Perlwitz, J.P., C. Perez Garcia-Pando, and R.L. Miller, 2016: Predicting the Mineral Composition of Dust Aerosols With an Earth System Model (NASA GISS ModelE2). Invited talk at King Abdullah University of Science and Technology, Thuwal, Saudi Arabia, 02/17/2016.

4. Perez Garcia-Pando, C., R.L. Miller, J.P. Perlwitz, and P. Ginoux, 2015. Global dust sources detection using MODIS Deep Blue Collection 6 aerosol products. (On behalf of Paul Ginoux) AGU Fall Meeting 2015, San Francisco, December 2015.

5. Perez Garcia-Pando, C., R.L. Miller, J.P. Perlwitz, 2015. Dust Composition in Climate Models: Current Status and Prospects. AGU Fall Meeting 2015, San Francisco, December 2015.

6. Perez Garcia-Pando, C., R.L. Miller, J.P. Perlwitz, 2015. Constraining the Dust Mineral Composition in Climate Models. Conference on Airborne Dust, Climate Change, and Human Health. Organized by Henry F. Diaz, Joseph M. Prospero and Roger S. Pulwarty. Miami, Florida. May 19?21, 2015.

7. Perez Garcia-Pando, C., 2015. Can We Inform Reactive Vaccination Strategies for Meningococcal Meningitis in Sub-Saharan Africa Using Dust and Climate Predictors? Conference on Human Health in the Face of Climate Change: Science, Medicine, and Adaptation. Organized by the ”la Caixa” Foundation, BIOCAT, and the New York Academy of Sciences. Barcelona, Spain. May 14 - 15, 2015

8. Perez Garcia-Pando, C., 2015. Using Brittle Fragmentation Theory to Estimate Aerosol Mineral Composition in Climate Models. Severo Ochoa Research Seminar Lectures. Barcelona Supercomputing Center. 26 March 2015.

9. Perez Garcia-Pando, C., 2015. Soil dust aerosols and wind as predictors of seasonal meningitis incidence in Niger. Climate and Health Seminar. Department of Environmental Health Sciences. Mailman School of Public Health, Columbia University (New York). February 27th, 2014.

10. Perez Garcia-Pando, C., 2015. Meningitis and Climate: From Science to Practice (a review). Workshop: 'Next Generation Modeling: Climate, Weather and Infectious Disease' organized at Princeton University by the NIH Fogarty International Center Research and Policy for Infectious Disease Dynamics (RAPIDD) program. Princeton University. 15-17 January 2014.

11. Perez Garcia-Pando, C., 2015. Mineral dust in Northern Africa. Concept Development Workshop: Impact of Saharan Dust Particles on Epidemic Bacterial Meningitis. Norwegian Institute of Public Health. Oslo, Norway. September 2013.

12. Perez Garcia-Pando, C., 2015. Meningitis and Climate: from Science to Practice. Concept Development Workshop: Impact of Saharan Dust Particles on Epidemic Bacterial Meningitis. Norwegian Institute of Public Health. Oslo, Norway. September 2013.

4.1.6 Conferences

1. Green, R., V. Realmuto, D. Thompson, N. Mahowald, C. Perez Garcia-Pando, R.L. Miller, R. Clark, G. Swayze, G. Okin, 2015. Advances in Mineral Dust Source Composition Measurement with Imaging Spectroscopy at the Salton Sea, CA. AGU Fall Meeting 2015. San Francisco. December 2015.

2. Miller, R.L., C. Perez Garcia-Pando, J.P. Perlwitz, 2015. Why Is Improvement of Earth System Models So Elusive? Challenges and Strategies From Dust Aerosol Modeling. AGU Fall Meeting. San Francisco. December 2015.
3. Perlwitz, J.P., C. Perez Garcia-Pando, R.L. Miller, A.M. Fridlind, and D.A. Knopf, 2015. How the Assumed Size Distribution of Dust Minerals Affects the Predicted Ice Forming Nuclei. AGU Fall Meeting. December 2015.

4. Basart, S., O. Jorba, C. Perez Garcia-Pando, C. Pringent, 2015. Modelling mineral dust emission over North Africa and Middle East using high-resolution surface properties from satellite retrieval. European Aerosol Conference, Milan, September 2015.

5. Perez Garcia-Pando, C., R.L. Miller, J.P. Perlwitz, 2014. Using Brittle Fragmentation Theory to represent Aerosol Mineral Composition. AGU Fall Meeting. San Francisco, 13-18 December 2014

6. Miller, R.L., C. Perez Garcia-Pando, J.P. Perlwitz, Paul Ginoux, 2014. Radiative Forcing and Perturbations To Climate By Anthropogenic Sources of Soil Dust Aerosols. AGU Fall Meeting. San Francisco, 13-18 December 2014

7. Perlwitz, J.P., C. Perez Garcia-Pando, R.L. Miller, 2014. Predicting the Mineral Composition of Dust Aerosols: Evaluation and Implications. AGU Fall Meeting. San Francisco, 13-18 December 2014.

8. Perez Garcia-Pando, M.C Thomson, M. Stanton, P.J. Diggle, R.L. Miller, J.P. Perlwitz, P. Ceccato, 2014. Informing Reactive Vaccination Strategies for Meningococcal Meningitis in sub-Saharan Africa using Dust and Climate Predictors. AGU Fall Meeting. San Francisco, 13-18 December 2014.

9. Perez Garcia-Pando, C., J.P. Perlwitz, R.L. Miller, 2014. New Methods to Predict the Mineral and Chemical Composition of Dust Aerosols. 13th AEROCOM Workshop. Steamboat Springs, Colorado. 28 September-2 October 2014.

10. Perez Garcia-Pando, C., J.P. Perlwitz, R.L. Miller, 2014. Constraining dust mineral and elemental composition in climate models. Department of Energy Climate Modeling PI Meeting. Bolger Conference Center, Potomac.

11. Perlwitz, J.P., C. Perez Garcia-Pando, R.L. Miller, 2014. From Mineral fractions in Soils To mineral fractions in Dust Aerosols ? an empirical approach for Models. DUST 2014 International Conference on Atmospheric Dust. Castellaneta Marina (Ta), Italy. June 1-6, 2014.

12. Basart, S., O. Jorba, C. Perez Garcia-Pando, C. Pringent, J.M. Baldasano, 2014. Modeling mineral dust emission over North Africa and Middle East using a new satellite surface properties database. DUST 2014 International Conference on Atmospheric Dust. Castellaneta Marina (Ta), Italy. June 1-6, 2014.

13. Basart, S., O. Jorba, C. Perez Garcia-Pando, C. Prigent, J.M Baldasano, 2014. Simulation of the mineral dust emission over Northern Africa and Middle East using an aerodynamic roughness length map derived from the ASCAT/PARASOL. European Geosciences Union, General Assembly 2014. Vienna, Austria. Apr. 27-May 2, 2014

14. Huneeus, N., S. Basart, S. Fiedler, J.-J. Morcrette, J. Mulcahy, E. Terradellas, C. Perez, G. Pejanovic, S. Nickovic, M. Schulz, J.M. Baldasano, A. Benedetti, E. Cuevas, J. Pey, 2014. Forecasting the North African dust outbreak towards Europe in April 2011: a model inter?comparison. MACC-II Open Science Conference. Brussels, Belgium. January 27-30, 2014.

15. Perez, C., R.L. Miller, J.P. Perlwitz, S. Rodrguez, 2013. Constraining the mineral and elemental composition of dust aerosol. Goldschmidt Conference 2013. Florence, Italy. August 25-30, 2013.

16. Menut, L., C. Perez, K. Haustein, B.B. Bessagnet, C. Prigent, S. Alfaro, 2012. Relative impact of roughness and soil texture on mineral dust emission fluxes modeling. AGU Fall Meeting. San Francisco, CA. December 3-7, 2012.

17. Miller, R.L, P. Knippertz, C. Perez, I. Tegen, 2012. The Comparative Influence of Aerosol Radiative Forcing at the Surface and Top of Atmosphere Upon the Hydrologic Cycle. AGU Fall Meeting. San Francisco, CA. December 3-7, 2012.

18. Perlwitz, J.P., C. Perez, R.L. Miller, S. Rodriguez, 2012. Predicting the Mineral Composition of Dust Aerosols. AGU Fall Meeting. San Francisco, CA. December 3-7, 2012.

19. Perlwitz, J.P., C. Perez, R.L. Miller, S. Rodriguez, 2012. Atmospheric iron from crustal sources: prognostic aerosol composition in GISS/ModelE. The 22nd Goldschmidt Conference. Montreal, Canada. June 24-29, 2012.

4.1.7 Web site or internet sites that reflect the results of this project

http://data.giss.nasa.gov/mineralfrac/

4.1.8 Networks/collaborations fostered

1. We submitted a proposal named 'EMIT' for the NASA Earth Venture Instrument-3 (EVI-3) program, whose team includes researchers from JPL, NASA GISS, NOAA GFDL and Cornell University. The project would directly measure the surface mineral composition at very high res-

olution (100m) by using imaging spectroscopy from the International Space Station (ISS), whose orbit provides ideal coverage for the dust source regions of the Earth. The modeling part of the proposal leverages on the techniques developed by this DoE funded project.

2. Collaboration with Stony Brook University on experimental investigation of the governing parameters of atmospheric ice nucleation using field-collected and laboratory generated aerosol particles and its application in cloud resolving models.

3. Collaboration with UC San Diego on synergistic investigation of dust mineral heterogeneous chemistry using laboratory measurements and an Earth system model.

4. Potential collaboration with General Electric on dust mineral heterogeneous chemistry.

5. Collaboration with LSCE in France to apply the techniques developed by this projects using a new soil mineralogy database.

4.1.9 Technologies/Techniques

New methods to simulate the mineral composition in Earth System models

4.1.10 Inventions/patents

All the techniques developed are open and not patented.

4.1.11 Other products such as databases, models

We have made available (at http://data.giss.nasa.gov/mineralfrac/) the data files containing the global distribution of the mineral fractions of dust aerosols at emission for the Soil Mineral Fraction (SMF) method and the Aerosol Mineral Fraction (AMF) method . Eight mineral species in five size ranges are considered. The mineral phases are illite (Illi), kaolinite (Kaol), smectite (Smec), carbonates (Calc), quartz (Quar), feldspar (Feld), iron oxides (FeOx), and gypsum (Gyps). The size ranges are 0.1-2 m (Clay), 2-4 μm (Silt1), 4-8 μm (Silt2), 8-16 μm (Silt3), and 16-32 μm (Silt4) particle diameter.

The method on which data in the files are based can be determined from the file name ('SMFmethod' or 'AMFmethod'). The files with '4320x2160' in the name contain the mineral fractions at emission at the native resolution of 5' longitude by 5' latitude. The files with '144x90' in the name are gridded at 2.5 longitude by 2 latitude resolution and are as used for model experiments using NASA GISS ModelE2. The lower resolution fields were derived by interpolation from the high-resolution fields.

The global compilation of observations is also available in the Supporting Information of Perlwitz et al. (2015b).

5 For projects involving computer modeling

5.1 Model description, key assumptions, version, source, and intended use

Our model of the emitted mineral fractions has been incorporated into the CMIP5 version of the NASA GISS Earth System ModelE2 (Schmidt et al., 2014) that has horizontal resolution of 2 latitude by 2.5 longitude and 40 vertical layers up to $0.1\,hPa$. The dust aerosol module that is largely unchanged since its description in Miller et al. (2006). In the NASA GISS ModelE, the emission of dust minerals occurs preferentially in arid topographic lows (Ginoux et al., 2001), and accounts both for subgrid scale wind variations (Cakmur et al. 2004), and the increase of threshold wind speeds with soil wetness (Shao et al., 1996). Dry removal occurs through turbulent deposition in the surface layer (Wesely and Hicks, 1977; Koch et al., 1999), and gravitational settling with settling speeds that are proportional to mineral density. All the minerals have similar densities, except iron oxides whose density is nearly twice the value of the other minerals. Wet deposition occurs through scavenging both within and below clouds where there is precipitating condensate, assuming that all minerals are 50% soluble (Koch et al., 1999).

The mathematical description of the methods to prescribe the size-distributed mineral fractions of dust is included below.

5.2 Performance criteria for the model to the intended use and test results to demonstrate the model performance criteria were met

Please see sections 3.4, 3.5 and 3.6 of this report and Perlwitz et al. (2015b)

5.3 Theory behind the model and mathematics to be used, including formulas and calculation methods

5.3.1 Semi-empirical model

We describe here our calculation of the emitted fraction of each mineral and its particle size distribution through the developed semi-empirical approach. An extensive description can be found in Perlwitz et al. (2015a). We treat the dust particles as an external mixture of minerals, each corresponding to a separate prognostic variable. We create additional prognostic variables for mixtures of each mineral with iron oxides, where the latter is assumed to be a small fraction of the total particle mass. Calculation of iron oxide mixtures is described separately in the next section.

We first derive the mineral composition of the fully dispersed soil following Claquin et al. (1999). Their MMT gives $f_n^c(a)$ and $f_n^s(a)$, the mass fraction of mineral n in the clay (0 to 2 μm) and silt (2 to 50 μm) size categories, respectively, as a function of α, the arid soil type, whose spatial distribution is provided by the Digital Soil Map of the World (FAO, 2007) that is integrated into the Harmonized World Soil Database (HWSD FAO/IIASA/ISRIC/ISSCAS/JRC, 2012). For each value of soil type α (that implicitly varies with location), the mineral fractions given by the MMT sum to unity:

$$\sum_{n}^{N} f_n^c(\alpha) = 1 \text{ and } \sum_{n}^{N} f_n^s(\alpha) = 1 \tag{3}$$

For Claquin et al. (1999), only calcite (or more generally, "carbonates") and quartz are present at all particle sizes. Phyllosilicates (illite, kaolinite, smectite) are present only at clay sizes, while feldspar, gypsum and hematite are restricted to silt sizes. Based upon measurements shown in Fig. 1, we assume that each mineral is present within all size categories, so that N, the total number of minerals, equals 8 for both clay and silt-sized particles. The fraction of hematite provided by the MMT was originally derived using soil redness and assigned to the silt size category without reference to its measured size distribution. However, soil measurements show that iron oxides like hematite are present over a range of diameters as small as nanometers. We assume that hematite is present at both clay and silt sizes, assuming that the clay fraction is identical to the silt fraction provided by the MMT. We assume that the hematite fraction that is newly introduced at clay sizes occurs at the expense of the phyllosilicate fractions within the MMT. This is partly because iron oxides are a weathering product of phyllosilicates, but in practice this offset causes only a small reduction of the phyllosilicate fraction.

To calculate the mineral fractions of the dispersed soil at each location, we specify the fraction of each size category present, provided by the soil texture class β, whose spatial distribution is provided by the FAO/STATSGO soil texture. Let $s^c(\beta)$ and $s^s(\beta)$ be the mass fractions of clay and silt-sized particles provided by the soil texture triangle for each soil texture class β. The clay and silt-size fractions are normalized to sum to unity at each location:

$$s^c(\beta) + s^s(\beta) = 1 \tag{4}$$

Thus, the soil mass fraction of each mineral in the clay and silt-size categories, s_n^c and s_n^s, respectively, is given by:

$$s_n^c(\alpha,\beta) = s^c(\beta) f_n^c(\alpha) \text{ and } s_n^s(\alpha,\beta) = s^s(\beta) f_n^s(\alpha) \tag{5}$$

As a result of Eqs. (3) and (4), the soil mass fractions sum to unity over all sizes and minerals:

$$\sum_{n}^{N} (s_n^c + s_n^s) = 1 \tag{6}$$

The soil mass fraction of each mineral varies regionally through its dependence upon the arid soil type α (through the MMT that gives the fractional mineral composition of each size category) and soil texture β (that gives the local fractional abundance of each size category). For brevity, we will hereafter omit the dependence of s_n^c and s_n^s upon α and β (and implicitly upon location).

We have derived Eq. (5), the mass fraction of each mineral within the dispersed soil, by applying the method of Claquin et al. (1999) with the extension of hematite to clay sizes. What remains is to specify the *emitted* fraction of each mineral within each size category.

Let a^c and a^s be the mass fractions of emitted clay and silt-sized aerosols, respectively, that at each location satisfy:

$$a^c + a^s = 1 \tag{7}$$

(The symbols "a" and "s" are chosen to signify the aerosol and soil, respectively.) We further decompose each aerosol mass fraction into contributions from the N minerals. Let a_n^c and a_n^s represent the contribution of mineral n to the mass fraction of emitted clay and silt-sized particles, respectively:

$$a^c = \sum_n^N a_n^c \text{ and } a^s = \sum_n^N a_n^s \tag{8}$$

that because of Eq. (7) satisfy:

$$\sum_n^N (a_n^c + a_n^s) = 1 \tag{9}$$

That is, the sum of the aerosol mineral fractions over all sizes and minerals equals unity.

We prescribe the mass fraction of the emitted clay-sized particles using brittle fragmentation theory:

$$a^c = 0.013 \tag{10}$$

We assume that a^c is independent of location, based upon Kok (2011), who argues that the black curve in Fig. 2 is a good approximation to measurements of the emitted size fraction for a variety of soils and wind conditions. As a consequence of Eqs. (5) and (10), the emission of clay-sized mineral n (excluding feldspar and gypsum) is:

$$a_n^c(\alpha) = a^c f_n^c(\alpha) \quad \text{where } a^c = 0.013. \tag{11}$$

Note that for emission at clay sizes, the proportion of minerals is identical to that of the fully dispersed soil and given by the MMT.

Because of Eq. (7), the emitted silt fraction a^s is implicitly determined:

$$a^s = 1 - a^c = 0.987. \tag{12}$$

As noted above, the assumption of an emitted size distribution that is spatially uniform is shared by many models.

We also assume that the emitted mass fraction of each mineral n at silt sizes (a_n^s) consists of two contributions from the wet-sieved soil. The emitted fraction combines soil mass at silt sizes along with clay particles whose aggregates were broken during wet sieving. This is expressed by Eq. (2), but we represent reaggregation more simply by augmenting emission at silt sizes in proportion to the fractional abundance of clay particles in the fully dispersed soil (s_n^c):

$$a_n^s = \eta(\gamma_n s_n^c + s_n^s). \tag{13}$$

Here, γ_n is a coefficient of proportionality that controls the magnitude of reaggregation and augmentation of the emitted silt fraction for mineral n. For simplicity, we assume that γ_n is identical for all reaggregated minerals, except for feldspar and gypsum, which must be treated separately as described below. The remaining exception is quartz, whose abundance at large diameters in Fig. 1 suggests that it experiences minimal dispersion, which we represent by setting $\gamma_n = 0$. The parameter η is calculated at each location to satisfy Eq. (12).

As a consequence of Eqs. (5) and (13), the emission of mineral n at silt sizes is:

$$a_n^s(\alpha,\beta) = \eta(\alpha,\beta)\left[\gamma_n s^c(\beta) f_n^c(\alpha) + s^s(\beta) f_n^s(\alpha)\right], \tag{14}$$

noting that $\gamma_n \equiv \gamma$, a constant that is identical for all minerals, except for quartz, for which $\gamma_n \equiv 0$. We have temporarily noted the dependence of the silt fraction a^s upon the local soil type α and texture β.

Equation 14 extends clay-sized minerals like phyllosilicates into the silt-size range, consistent with measurements by Kandler et al. (2009), illustrated in Fig. 1. This extension increases in proportion to the clay fraction of the fully dispersed soil, a heuristic representation of (2).

Because the total fractional silt emission is assumed to be fixed according to Eq. (12), γ has the effect of reducing the fractional emission of minerals like quartz that are predominantly silt-sized in the dispersed soil.

Feldspar and gypsum are observed as aerosols at both clay and silt sizes (Fig. 1). Because of the absence of each mineral at clay sizes within the MMT, we cannot specify the emitted clay fraction using Eq. (11). Instead, we assume that the emitted silt mass of each mineral (a_n^s) is closely related to its soil mass fraction (s_n^s). Then, we calculate the emitted clay mass using its ratio (ψ_n) with respect to the emitted silt mass:

$$a_n^c = \psi_n a_n^s \tag{15}$$

where:

$$a_n^s = \eta(\alpha,b) s^s(b) f_n^s(\alpha) \tag{16}$$

and n corresponds to feldspar and gypsum. The ratio ψ_n is given by the measured volume distribution after adjusting for modification of the emitted size distribution at small diameters during transport to Tinfou. We proportionally reduce the soil fractions of illite, smectite and kaolinite at clay sizes to compensate for the reintroduction of emitted feldspar and gypsum at this size. (This is an alternative to reducing all the soil mineral fractions at clay sizes. We justify this approximation as a result of the predominance of phyllosilicates at this size according to the MMT.)

The emitted silt particles have diameters ranging between 2 and 50 μm (consistent with the MMT). We distribute each mineral's silt particles over the size categories transported by ModelE2. (Clay-sized particles are transported in a single bin by ModelE2, so distribution within this size range is unnecessary.) We introduce an additional model size category between 32 and 50 μm that is not

transported so that the total silt size range within the model and MMT are identical. Let $a^s_{n,k}$ be the emitted mass fraction of mineral n within size category k. To distribute the silt mass, we use the normalized mass distribution of each mineral derived from measurements during SAMUM. We define $m^s_{n,k}$ as the mass fraction within size bin k that is normalized for each mineral n over the MMT silt range (between 2 and 50 μm) so that:

$$\sum_{k \in \substack{\text{all silt} \\ \text{size bins}}} m^s_{n,k} = 1 \text{ for each mineral } n. \tag{17}$$

Then, the emitted mineral fraction within each silt size bin k is:

$$a^s_{n,k} = a^s_n m^s_{n,k} \tag{18}$$

Finally, we renormalize the mass fractions a^c_n and $a^s_{n,k}$ so that their sum over all minerals and sizes is unity for diameters up to 32 μm. (Silt particles with diameters between 32 and 50 μm are not transported by the model.) This renormalization has the effect of reducing the fraction of quartz compared to the MMT. This is because a greater mass fraction of quartz is measured at diameters above 32 μm, compared to other minerals. For example, quartz has 38 % of its mass between 32 and 50μm, a significantly larger amount than that of carbonates (23 %), feldspar (30 %) and particularly gypsum (2 %). The shift of quartz aerosols toward larger diameters compared to other minerals results from the larger characteristic particle size of quartz in the parent soil. Thus, the fractional emission of quartz at silt sizes is reduced by two effects compared to the fraction indicated by the MMT: first, the reconstruction of emitted aggregates at silt sizes from wet-sieved clay-sized particles, and second, the limited size range of our transport model. The second effect is ultimately the result of a disproportionate mass of quartz at diameters that are too large to travel far from their source.

5.3.2 Iron oxides as internal mixtures

In our model, iron oxides can travel either in pure crystalline form or as an internal mixture with other minerals. (Combinations of the other minerals excluding iron oxides are treated as external mixtures.). We refer to the iron oxide within an internal mixture as an "accretion". (We avoid referring this mixture as an aggregate to avoid confusion with the more general class of aggregated minerals that are subject to brittle fragmentation.)

At each location, Eqs. (11) and (14), along with (15) and (16), give us $a^c_{n,k}$ and $a^s_{n,k}$, including the mass fraction of emitted iron oxide. To create mixtures with other minerals, we specify the hematite fraction available for mixing along with its mass fraction in each particle. (We describe mixtures in terms of "iron oxides" rather than hematite, whose fraction is provided by the MMT, because our mixing method applies to other highly weathered iron minerals like goethite that are frequently found in aggregation.)

To simplify notation, we drop the superscripts in Eqs. (11), (14), (15) and (16) that distinguish between clay and silt-sized particles, and denote particle size solely through the k index of $a_{n,k}$. For the GISS ModelE2, $k = 1$ corresponds to the clay-sized fraction, while transported silt sizes

correspond to k equal 2 through 5.

We first distinguish between each mineral in its pure and mixed state:

$$a_{n,k} = a_{n,k}^{\text{pure}} + a_{n,k}^{\text{mix}} \tag{19}$$

For the particular case of iron oxides, we replace the mineral index n with Fe, so that $a_{Fe,k}$ denotes the emitted mass fraction of iron oxide in size category k. Then, analogous to Eq. (19), iron oxides can be decomposed into pure crystals and impurities mixed with other minerals:

$$a_{Fe,k} = a_{Fe,k}^{\text{pure}} + a_{Fe,k}^{\text{mix}} \tag{20}$$

We further distinguish the mixture of iron oxide among the remaining minerals (each denoted by the subscript n) as $a_{Fe|n,k}^{\text{mix}}$, so that the total iron oxide within mixtures is the sum over n:

$$a_{Fe,k}^{\text{mix}} = \sum_{n \neq \text{iron oxide}} a_{Fe|n,k}^{\text{mix}} \tag{21}$$

We determine $a_{Fe|n,k}^{\text{mix}}$ by first specifying the fraction of emitted iron oxide available for mixing. Define ε as the fraction of iron oxide emitted as pure crystals:

$$a_{Fe,k}^{\text{pure}} = \varepsilon a_{Fe,k} \tag{22}$$

Micrometer-sized crystalline iron oxide aggregates are typically observed in highly weathered soils that are rich in iron oxides. Therefore, we assume that the amount of crystalline iron oxides not attached as small impurities to other minerals is proportional to the total iron oxide content of the soil, so that ε is proportional to the total iron oxide:

$$\varepsilon = \varepsilon_0 a_{Fe,k} \tag{23}$$

Then:

$$a_{Fe,k}^{\text{pure}} = \varepsilon_0 a_{Fe,k}^2 \tag{24}$$

and using Eq. (20):

$$a_{Fe,k}^{\text{mix}} = (1-\varepsilon) a_{Fe,k} = (1 - \varepsilon_0 a_{Fe,k}) a_{Fe,k} \tag{25}$$

Equation (23) expresses our assumption that the fraction of pure crystalline iron oxide increases where the total iron oxide fraction is large, a heuristic attempt to account for the weathering that creates iron oxides in the soil. As a soil weathers, more of the primary and secondary Fe-bearing minerals decompose and the iron within the mineral lattices is converted to iron oxides in the soil. In absence of quantitative observational constraints, we simply set $\varepsilon_0 = 1$. In the future, ε_0 could be prescribed differently or even be a function of other soil properties.

We next assume that iron oxide is mixed with the other minerals in proportion R to the total particle mass:

$$a_{Fe|n,k}^{\text{mix}} = R \left(a_{n,k}^{\text{mix}} + a_{Fe|n,k}^{\text{mix}} \right). \tag{26}$$

We assume that R is a small number so that the iron oxides only slightly perturb the density of the mixture. We set R equal to 0.05, but are aware of only a few measurements that would guide a more precise choice of this parameter.

Finally, we assume that the iron oxide available for mixing is distributed among the other minerals in proportion to their mass fraction:

$$a_{Fe|n,k}^{\text{mix}} \propto \frac{a_{n,k}}{\overline{a}_k} \tag{27}$$

where $\overline{a}_k$ is the mass fraction for each size category summed over all minerals except for iron oxide.

$$\overline{a}_k = \sum_{n \neq \text{iron oxide}} a_{n,k} \tag{28}$$

Equation (27) is a reasonable first assumption, although future efforts might construct mixtures by considering whether iron oxides are more likely to be created by weathering of specific minerals. For example, iron oxides and clay minerals are formed during chemical weathering of parent minerals and are in intimate physical association with each other.

As a result of Eqs. (25) and (27):

$$a_{Fe|n,k}^{\text{mix}} = \left(1 - a_{Fe,k}\right) a_{Fe,k} \frac{a_{n,k}}{\overline{a}_k} \tag{29}$$

Based on these assumptions it can be shown that the emitted mass fraction of iron oxide mixed with mineral n is:

$$a_{n,k}^{\text{mix}} + a_{Fe|n,k}^{\text{mix}} = \min\left[\frac{\left(1 - a_{Fe,k}\right) a_{Fe,k}}{R} \frac{a_{n,k}}{\overline{a}_k}, \frac{a_{n,k}}{1-R}\right]. \tag{30}$$

The second term within the minimum results from the possibility that for small enough mass fractions of accreted iron oxide within each particle ($R \ll 1$), there will be insufficient amounts of mineral n available for combination with the amount of iron oxide specified by Eq. (25).

The mass fraction of pure, crystalline iron oxide is given by:

$$a_{Fe,k}^{\text{pure}} = a_{Fe,k} - \min\left[(1 - a_{Fe,k}) a_{Fe,k}, \frac{R}{1-R} \overline{a}_k\right], \tag{31}$$

while the mass fraction of pure mineral n is given by:

$$a_{n,k}^{\text{pure}} = a_{n,k} - \left(\frac{1-R}{R}\right) a_{Fe|n,k}^{\text{mix}}. \tag{32}$$

According to Eq. (26), iron oxides are accreted with host minerals within the same size category k. This follows from our interpretation of $a_{Fe|n,k}^{\text{mix}}$ as the mass fraction of iron oxides within

these particle combinations, whose size category k indicates the diameter of the combined particle. This diameter mainly reflects the contribution of the host mineral n, given our assumption that the fractional contribution R of iron oxide mass to the combined particle is small. The accreted fraction $a^{\text{mix}}_{Fe|n,k}$ represents the small crystals of iron oxides attached to the host mineral as seen in single-particle images. We emphasize that these iron oxides available for mixing are not particles themselves with diameters within the size category k. In contrast, the fraction of pure, crystalline iron oxides ($a^{\text{pure}}_{n,k}$) that does not combine with other minerals has a particle diameter within size category k. Our modeling assumptions leading to Eq. (30) should be evaluated with more measurements of the size distribution and mixing state of iron oxides in the soil.

5.3.3 Theoretical model

We describe here our calculation of the emitted fraction of each mineral and its particle size distribution based on extensions of brittle fragmentation theory. This method hasn't been peer reviewed yet. The related publication is in preparation.

The basic theory of Kok

When a brittle material such as glass or gypsum receives a large input of energy, the resulting fragment particle size distribution (PSD) can be classified into three regimes: elastic regime, damage regime and fragmentation regime. Kok (2011) assumes that dust emission is predominantly due to fragmenting impacts, i.e. the object fragments into a wide range of particle sizes and the size of the largest fragment is small compared to that of the original object. Measurements show that the number of fragments with size D_f can be described as:

$$\frac{dN_f}{d\ln D_f} \propto D_f^{-2} \exp\left[(-\left(\frac{D_f}{\lambda}\right)^3\right] \quad (D_f > x_0) \tag{33}$$

where λ is side crack propagation length (generally on the order of 10% of the size of the original object) and x_0 the indivisible constituent size (10^{-7}–10^{-5} m for dust).

Dust aerosols are aggregates themselves such that an emitted dust aerosol consists of one or more soil particles of equal or smaller size. Kok assumes that the production of dust aerosols with size D_d is proportional to the volume fraction of soil particles with size $D_s \leq D_d$,

$$\frac{dN_d}{d\ln D_d} \propto \int_0^{D_d} P_s(D_s)\, dD_s \tag{34}$$

where N_d is the normalized nunber of emitted dust aerosols with size D_d and P_s is the fully dispersed PSD of PM20 soil particles. Kok describes the distribution of fully disagregated (dispersed or disturbed) soil particles using a monomodal log-normal distribution:

$$P_s(D_s) = \frac{dV_s}{d\ln D_s} = \frac{1}{\sqrt{2\pi}\ln(\sigma_s)} \exp\left[-\frac{\ln^2(D_s/\bar{D}_s)}{2\ln^2(\sigma_s)}\right] \tag{35}$$

where σ_s is the geometric standard deviation and $\bar{D}_s$ is the volume median diameter. Combining

(33), (34) and (35) the normalized number and volume size distributions are derived:

$$\frac{dN_d}{d\ln D_d} = \frac{1}{2C_N D_d^2}\left[1+erf\left(\frac{\ln(D_d/\bar{D}_s)}{\sqrt{2}\ln(\sigma_s)}\right)\right]\exp\left[-\left(\frac{D_d}{\lambda}\right)^3\right] \tag{36}$$

$$\frac{dV_d}{d\ln D_d} = \frac{D_d}{2C_V}\left[1+erf\left(\frac{\ln(D_d/\bar{D}_s)}{\sqrt{2}\ln(\sigma_s)}\right)\right]\exp\left[-\left(\frac{D_d}{\lambda}\right)^3\right] \tag{37}$$

where erf is the error function and C_N and C_V are normalization constants calculated as

$$C_N = \int_0^{20}\frac{1}{2D_d^3}\left[1+erf\left(\frac{\ln(D_d/\bar{D}_s)}{\sqrt{2}\ln(\sigma_s)}\right)\right]\exp\left[-\left(\frac{D_d}{\lambda}\right)^3\right]dD_d \tag{38}$$

$$C_V = \int_0^{20}\frac{1}{2}\left[1+erf\left(\frac{\ln(D_d/\bar{D}_s)}{\sqrt{2}\ln(\sigma_s)}\right)\right]\exp\left[-\left(\frac{D_d}{\lambda}\right)^3\right]dD_d \tag{39}$$

There are few published arid soil PSDs that extend into the submicron range. One exception is the study of D'Almeida and Schutz (1983) who report PSDs for six arid soils across the Sahara and the study of Goldstein et al. (2005) who report PSDs for 2 soil in Utah. By applying a least-squares fitting technique Kok determined the most likely values of the log-normal parameters $\bar{D}_s$ and σ_s for each individual soil ($\bar{D}_s = 3.4 \pm 1.8\mu$m and $\sigma_s = 3.0 \pm 0.4$). $\bar{D}_s$ in these soils range from 1.6 to 7.2 μm and σ_s from 2.8 to 3.7. With these values, a side crack propagation length $\lambda = 12 \pm 1\mu m$ is obtained by performing a least-squares fit to measurements of the emitted size distribution.

Extending Kok's model to use varying FAO soil textures

The goal is to derive an emitted size distribution for each mineral and arid soil type and soil texture. In this section we first apply Kok's model for the total dust emission using the PSD's from global estimates of the mass fractions of clay and silt in the soil. An important aspect of this methodology is that Kok's theory uses the fully dispersed PSD of the soil. The FAO estimates are based on measurements performed by wet sedimentation techniques which break the soil aggregates which lead to relatively high amounts of loose clay particles that generally form aggregates of larger size. For this reason FAO estimates are well suited to be used with Kok's approach.

For the calculation of the soil PSD's we can use the mass fractions of clay and silt in the soil assuming bimodal (with bounded or unbounded modes) or monomodal log-normal distributions. In the FAO estimates, clay ranges from 0 to 2 μm and silt ranges from 2 to 50 μm. The most convenient approach is to fit the FAO soil fraction estimates of clay and silt to monomodal log-normal distributions. Let $P_s(D_s)$ be the normalized volume (mass) PSD of a soil with median diameter $\bar{D}_s$ and geometric standard deviation σ_s, then: (c_v is the normalization constant between 0 and 50 μm)

$$P_s(D_s) = \frac{1}{c_v\sqrt{2\pi}\ln(\sigma_s)}\exp\left[-\frac{\ln^2(D_s/\bar{D}_s)}{2\ln^2(\sigma_s)}\right] \tag{40}$$

$$c_v = \int_0^{50} \frac{1}{\sqrt{2\pi}\ln(\sigma_s)D_s} \exp\left[-\frac{\ln^2(D_s/\bar{D}_s)}{2\ln^2(\sigma_s)}\right] dD_s \tag{41}$$

Then, $\bar{D}_s$ and σ_s can be fitted by numerically solving:

$$\frac{1}{2c_v}\left(1 + erf\left[\frac{\ln(2/\bar{D}_s)}{\sqrt{2}\ln(\sigma_s)}\right]\right) = f_c \tag{42}$$

$$\frac{1}{2c_v}\left(erf\left[\frac{\ln(50/\bar{D}_s)}{\sqrt{2}\ln(\sigma_s)}\right] - erf\left[\frac{\ln(2/\bar{D}_s)}{\sqrt{2}\ln(\sigma_s)}\right]\right) = f_s \tag{43}$$

where f_c and f_s are the known soil fractions of clay and silt. The fitted values are displayed in Table 1. A interesting result is to see that the range of values in Table 1 from FAO soil textures is equivalent to the range of values found by Kok (2011) when fitting a log-normal distribution to soil PSD measurements of specific soils.

Table 1: Fitted $\bar{D}_s$ and σ_s for the 12 FAO soil texture classes. λ_1 is the best fit to eq (37) without renormalization of the observations. λ_2 is the best fit to eq (37) with renormalization of the observations.

Soil texture class	Best fit $\bar{D}_s$	Best fit σ_s	Best fit λ_1	Best fit λ_2
Sand	2.75	2.70	10.8	10.8
Loamy Sand	3.55	3.59	13.3	11.0
Sandy Loam	5.45	3.80	11.8	10.7
Silt Loam	8.65	3.90	10.5	10.5
Silt	7.50	2.29	3.6	10.2
Loam	4.00	3.91	14.6	10.9
Sandy Clay Loam	1.25	3.66	40.0	12.4
Silty Clay Loam	2.80	2.91	11.4	11.1
Clay Loam	2.00	2.00	10.0	11.3
Sandy Clay	0.90	2.00	14.7	12.1
Silty Clay	2.00	2.00	10.0	11.3
Clay	0.95	3.12	40.0	12.7
Average and standard deviation	3.48 ± 2.53	2.99 ± 0.78	15.89 ± 11.62	11.25 ± 0.77

Fitting the side crack propagation length

Figure 2 in Kok (2011) shows that there is a small amount of scatter between the dust size flux datasets, even though these data were obtained for widely varying wind and soil conditions. This similarity suggests that changes in the wind and soil conditions have only a limited effect on the emitted dust PSD, as also suggested by the insensitivity of dust aerosol PSDs to changes in wind speed and source region. We therefore fitted λ by least squares for each of the soil texture classes with the derived numerical values of the observations in Kok (2011, Figure 2). Because measurements follow the power law of 1 in the range of 2-10 μm, Kok (2011) fitted each set of measurements in that size range for a given soil and a given wind speed to this power law. Then, Kok (2011) normalized the measurements at all aerosol sizes for this given soil and wind speed by

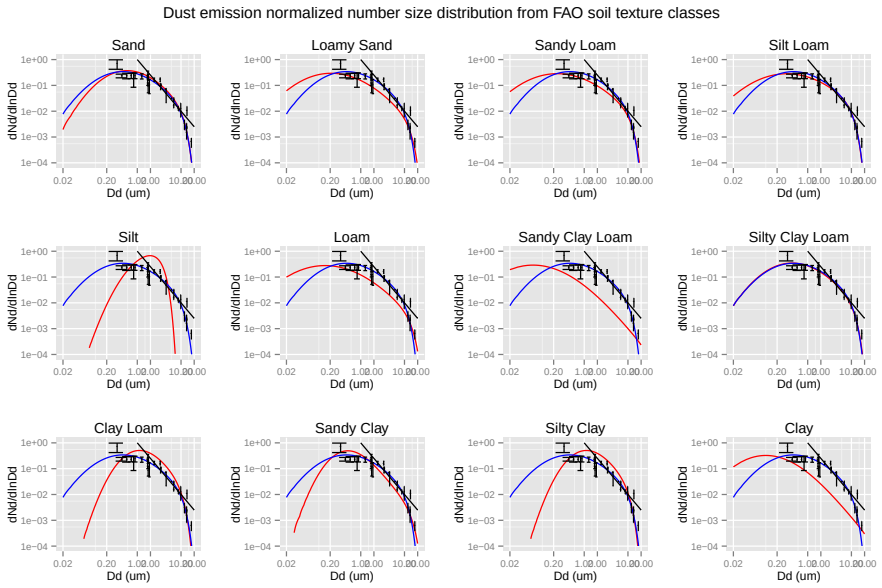

Figure 10: *Normalized number size distributions from the refitted Kok's model with average soil PSD (blue) and for fitted monomodal soil PSD's from FAO soil texture classes ($\lambda = \lambda_1$ (Table 1)) (red). σ_s and $\bar{D}_s$ for each soil texture class are listed in Table 1. The measurements and their error bars are shown in black. Also shown in black a line showing the power law of 1. For this case the dust size distribution of observations were not renormalized.*

the proportionality constant in the fitted power law. This means that the normalization of the measurements was also fitted together with λ. This implies that for each soil type, the measurements need to be renormalized (this is possible because we do not know the size distribution of emitted dust below 0.3 μm).

Figures 10 and 11 display the number size distributions for each soil texture class using the properties shown in Table 1. Figure 10 was produced without renormalization of the measurements (with best fit λ_1 in Table 1) and Figure 11 was produced with renormalization of the measurements (with best fit λ_2 in Table 1). It can be clearly seen that if measurements are not renormalized the model of Kok does not provide a good fit to the data and estimates of λ span a wide range of values (note that some values of λ_1 are 40 μm which indicates the sum of the residuals to the power of 2 is a decreasing function of λ). When the normalization constant of the measurements is fitted together with λ (λ_2 in Table 1), the model is a good fit of the data. Note also that the estimated $\lambda_2 = 11.25$ μm $\pm$ 0.77 is similar for all soils and consistent with the results of Kok.

Finally, Figure 12 displays the volume size distributions for each soil texture class using the properties shown in Table 1 with λ_2. All the estimated dust size distributions from different are a good fit of the observed data and λ is fairly similar. At the same time the differences of the estimated size distributions from different soils reflect the soil texture of the soil.

Extending Kok's model to use varying FAO soil textures and Claquin's mineral soil fractions

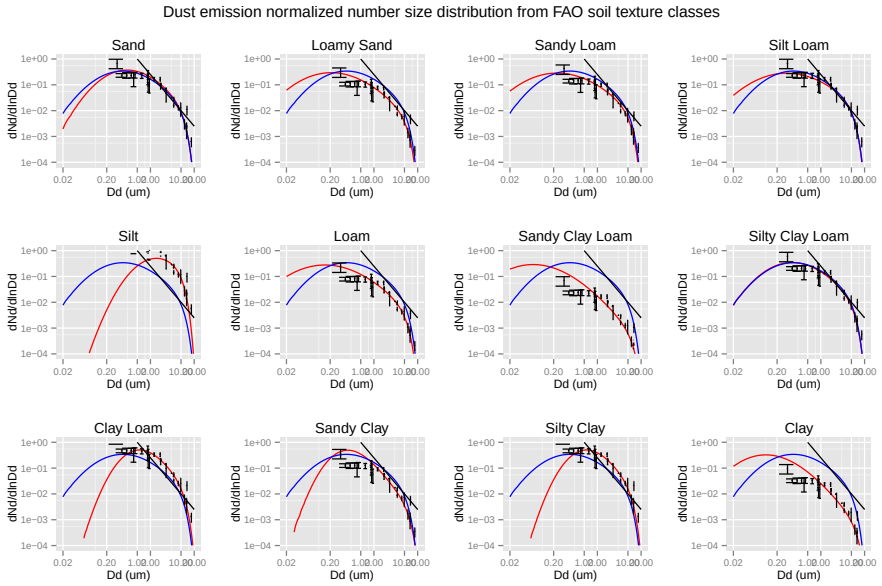

Figure 11: *Normalized number size distributions from the refitted Kok's model with average soil PSD (blue) and for fitted monomodal soil PSD's from FAO soil texture classes ($\lambda = \lambda_2$ (Table 1)) (red). σ_s and $\bar{D}_s$ for each soil texture class are listed in Table 1. The measurements and their error bars are shown in black. Also shown in black a line showing the power law of 1. For this case the dust size distribution of observations were renormalized to provide the best fit.*

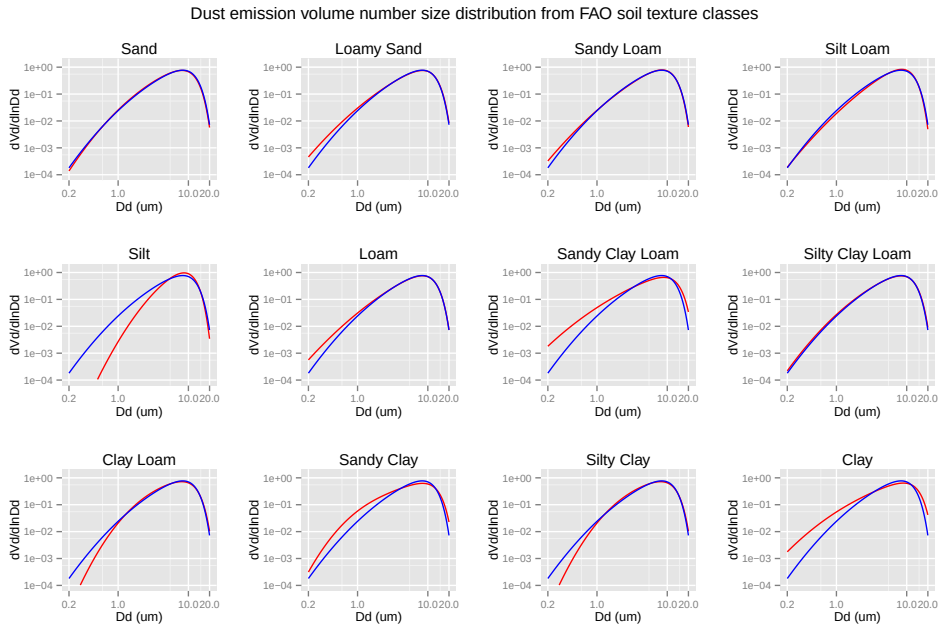

Figure 12: *Normalized volume size distributions from the refitted Kok's model with average soil PSD (blue) and for fitted monomodal soil PSD's from FAO soil texture classes ($\lambda = \lambda_2$ (Table 1)) (red). σ_s and $\bar{D}_s$ for each soil texture class are listed in Table 1.*

The fitted PSD's are now used to derive the normalized number and volume dust emitted size distributions:

$$\frac{dN_d}{d\ln D_d} = \frac{f_c}{2c_v C_N D_d^2}\left[1+erf\left(\frac{\ln(D_d/\bar{D}_s)}{\sqrt{2}\ln(\sigma_s)}\right)\right]\exp\left[-\left(\frac{D_d}{\lambda}\right)^3\right] \quad (0<D_d<2\mu m) \tag{44}$$

$$\frac{dN_d}{d\ln D_d} = \frac{f_c}{2c_v C_N D_d^2}\left[1+erf\left(\frac{\ln(2/\bar{D}_s)}{\sqrt{2}\ln(\sigma_s)}\right)\right]\exp\left[-\left(\frac{D_d}{\lambda}\right)^3\right]+ \frac{f_s}{2c_v C_N D_d^2}\left[erf\left(\frac{\ln(D_d/\bar{D}_s)}{\sqrt{2}\ln(\sigma_s)}\right)-erf\left(\frac{\ln(2/\bar{D}_s)}{\sqrt{2}\ln(\sigma_s)}\right)\right]\exp\left[-\left(\frac{D_d}{\lambda}\right)^3\right] \quad (2<D_d<20\mu m) \tag{45}$$

$$\frac{dV_d}{d\ln D_d} = \frac{f_c D_d}{2c_v C_V}\left[1+erf\left(\frac{\ln(D_d/\bar{D}_s)}{\sqrt{2}\ln(\sigma_s)}\right)\right]\exp\left[-\left(\frac{D_d}{\lambda}\right)^3\right] \quad (0<D_d<2\mu m) \tag{46}$$

$$\frac{dV_d}{d\ln D_d} = \frac{f_c D_d}{2c_v C_V}\left[1+erf\left(\frac{\ln(2/\bar{D}_s)}{\sqrt{2}\ln(\sigma_s)}\right)\right]\exp\left[-\left(\frac{D_d}{\lambda}\right)^3\right]+ \frac{f_s D_d}{2c_v C_V}\left[erf\left(\frac{\ln(D_d/\bar{D}_s)}{\sqrt{2}\ln(\sigma_s)}\right)-erf\left(\frac{\ln(2/\bar{D}_s)}{\sqrt{2}\ln(\sigma_s)}\right)\right]\exp\left[-\left(\frac{D_d}{\lambda}\right)^3\right] \quad (2<D_d<20\mu m) \tag{47}$$

where C_N and C_V are normalization constants.

Claquin et al. (1999) provided a Mean Mineralogical Table (MMT) as a function of FAO soil type. Let mc_i be the mass fraction of mineral i in the clay fraction, and ms_i the mass fraction of mineral i in the silt fraction, for $i = 1,..,8$. Note that mc =0 for Illite, Kaolinite, and Smectite, and ms =0 for Feldspar, Hematite and Gypsum. To derive normalized number and volume size distributions for each emitted mineral we extend Kok's model by assuming that aggregates are homogeneous mixtures of minerals with similar fragmentation properties. With this assumption (limitation) in mind we can derive the size distribution for each mineral i (for each soil type and soil texture):

$$\frac{dN_{di}}{d\ln D_d} = \frac{f_c mc_i}{2c_v C_{Ni} D_d^2}\left[1+erf\left(\frac{\ln(D_d/\bar{D}_s)}{\sqrt{2}\ln(\sigma_s)}\right)\right]\exp\left[-\left(\frac{D_d}{\lambda}\right)^3\right] \quad (0<D_d<2\mu m) \tag{48}$$

$$\frac{dN_{di}}{d\ln D_d} = \frac{f_c mc_i}{2c_v C_{Ni} D_d^2}\left[1+erf\left(\frac{\ln(2/\bar{D}_s)}{\sqrt{2}\ln(\sigma_s)}\right)\right]\exp\left[-\left(\frac{D_d}{\lambda}\right)^3\right]+$$
$$\frac{f_s ms_i}{2c_v C_{Ni} D_d^2}\left[erf\left(\frac{\ln(D_d/\bar{D}_s)}{\sqrt{2}\ln(\sigma_s)}\right)-erf\left(\frac{\ln(2/\bar{D}_s)}{\sqrt{2}\ln(\sigma_s)}\right)\right]\exp\left[-\left(\frac{D_d}{\lambda}\right)^3\right]$$
$$(2 < D_d < 20\mu m) \quad (49)$$

$$\frac{dV_{di}}{d\ln D_d} = \frac{f_c mc_i D_d}{2c_v C_{Vi}}\left[1+erf\left(\frac{\ln(D_d/\bar{D}_s)}{\sqrt{2}\ln(\sigma_s)}\right)\right]\exp\left[-\left(\frac{D_d}{\lambda}\right)^3\right] \quad (0 < D_d < 2\mu m) \quad (50)$$

$$\frac{dV_{di}}{d\ln D_d} = \frac{f_c mc_i D_d}{2c_v C_{Vi}}\left[1+erf\left(\frac{\ln(2/\bar{D}_s)}{\sqrt{2}\ln(\sigma_s)}\right)\right]\exp\left[-\left(\frac{D_d}{\lambda}\right)^3\right]+$$
$$\frac{f_s ms_i D_d}{2c_v C_{Vi}}\left[erf\left(\frac{\ln(D_d/\bar{D}_s)}{\sqrt{2}\ln(\sigma_s)}\right)-erf\left(\frac{\ln(2/\bar{D}_s)}{\sqrt{2}\ln(\sigma_s)}\right)\right]\exp\left[-\left(\frac{D_d}{\lambda}\right)^3\right]$$
$$(2 < D_d < 20\mu m) \quad (51)$$

Specifying soil size distributions for each mineral

One of the limitations of the previous methodology is that the shape of the soil size distributions of each mineral are assumed equal. By following this assumption the model predicts larger emitted quartz fractions in the silt sizes than observed. In this sense the soil size distributions for each mineral need to be considered independently. In this case we can fit independently the median diameter of the minerals that expand the clay and silt sizes assuming a mono modal distribution for each one. In the case of clay minerals for which there is only clay fraction we must assume those parameters a priori (we have assumed a median diameter of 1 μm and a geometric standard deviation of 2).

Then, for Illite, Smectite and Kaolinite:

$$P_{s_i}(D_s) = \frac{f_c mc_i}{c_{v_i}\sqrt{2\pi}\ln(\sigma_{sc})}\exp\left[-\frac{\ln^2(D_s/\bar{D}_{sc})}{2\ln^2(\sigma_{sc})}\right] \quad (0 < D_s < 2\mu m) \quad (52)$$

$$c_{v_i} = \int_0^2 \frac{1}{\sqrt{2\pi}\ln(\sigma_{sc})D_s}\exp\left[-\frac{\ln^2(D_s/\bar{D}_{sc})}{2\ln^2(\sigma_{sc})}\right] dD_s \quad (53)$$

For Calcite, Quartz, Feldspar, Gypsum and Hematite, we fit mono modal soil distributions of the form:

$$P_{s_i}(D_s) = \frac{f_c mc_i + f_s ms_i}{c_{v_i}\sqrt{2\pi}\ln(\sigma_{s_i})}\exp\left[-\frac{\ln^2(D_s/\bar{D}_{s_i})}{2\ln^2(\sigma_{s_i})}\right] \quad (0 < D_s < 50\mu m) \quad (54)$$

$$c_{v_i} = \int_0^{50} \frac{1}{\sqrt{2\pi}\ln(\sigma_{s_i})D_s} \exp\left[-\frac{\ln^2(D_s/\bar{D}_{s_i})}{2\ln^2(\sigma_{s_i})}\right] dD_s \tag{55}$$

Then, $\bar{D}_{s_i}$ and σ_{s_i} can be fitted by numerically solving:

$$\frac{1}{2c_{v_i}}\left(1+erf\left[\frac{\ln(2/\bar{D}_{s_i})}{\sqrt{2}\ln(\sigma_{s_i})}\right]\right) = \frac{\%Claymc_i}{\%Claymc_i+\%Siltms_i} \tag{56}$$

$$\frac{1}{2c_{v_i}}\left(erf\left[\frac{\ln(50/\bar{D}_{s_i})}{\sqrt{2}\ln(\sigma_{s_i})}\right]-erf\left[\frac{\ln(2/\bar{D}_{s_i})}{\sqrt{2}\ln(\sigma_{s_i})}\right]\right) = \frac{\%Siltms_i}{\%Claymc_i+\%Siltms_i} \tag{57}$$

With this approach the emitted size distributions for illite, kaolinite and smectite are

$$\frac{dN_{di}}{d\ln D_d} = \frac{f_c mc_i}{2c_{v_i}C_N D_d^2}\left[1+erf\left(\frac{\ln(D_d/\bar{D}_{s_i})}{\sqrt{2}\ln(\sigma_{s_i})}\right)\right]\exp\left[-\left(\frac{D_d}{\lambda}\right)^3\right] \quad (0<D_d<2\mu m) \tag{58}$$

$$\frac{dN_{di}}{d\ln D_d} = \frac{f_c mc_i}{2c_{v_i}C_N D_d^2}\left[1+erf\left(\frac{\ln(2/\bar{D}_{s_i})}{\sqrt{2}\ln(\sigma_{s_i})}\right)\right]\exp\left[-\left(\frac{D_d}{\lambda}\right)^3\right] \quad (2<D_d<20\mu m) \tag{59}$$

$$\frac{dV_{di}}{d\ln D_d} = \frac{f_c mc_i D_d}{2c_{v_i}C_V}\left[1+erf\left(\frac{\ln(D_d/\bar{D}_{s_i})}{\sqrt{2}\ln(\sigma_{s_i})}\right)\right]\exp\left[-\left(\frac{D_d}{\lambda}\right)^3\right] \quad (0<D_d<2\mu m) \tag{60}$$

$$\frac{dV_{di}}{d\ln D_d} = \frac{f_c mc_i D_d}{2c_{v_i}C_V}\left[1+erf\left(\frac{\ln(2/\bar{D}_{s_i})}{\sqrt{2}\ln(\sigma_{s_i})}\right)\right]\exp\left[-\left(\frac{D_d}{\lambda}\right)^3\right] \quad (2<D_d<20\mu m) \tag{61}$$

For Calcite, Quartz, Feldspar, Gypsum and Hematite

$$\frac{dN_{di}}{d\ln D_d} = \frac{f_c mc_i + f_s ms_i}{2c_{v_i}C_N D_d^2}\left[1+erf\left(\frac{\ln(D_d/\bar{D}_{s_i})}{\sqrt{2}\ln(\sigma_{s_i})}\right)\right]\exp\left[-\left(\frac{D_d}{\lambda}\right)^3\right] \quad (0<D_d<20\mu m) \tag{62}$$

$$\frac{dV_{di}}{d\ln D_d} = \frac{(f_c mc_i + f_s ms_i)D_d}{2c_{v_i}C_V}\left[1+erf\left(\frac{\ln(D_d/\bar{D}_{s_i})}{\sqrt{2}\ln(\sigma_{s_i})}\right)\right]\exp\left[-\left(\frac{D_d}{\lambda}\right)^3\right] \quad (0<D_d<20\mu m) \tag{63}$$

where

$$C_N = \sum_{i=1}^{3} \int_0^2 \frac{f_c mc_i}{2D_d^3} \left[1 + erf\left(\frac{\ln(D_d/\bar{D_s})}{\sqrt{2}\ln(\sigma_s)}\right)\right] \exp\left[-\left(\frac{D_d}{\lambda}\right)^3\right] dD_d$$
$$+ \sum_{i=1}^{3} \int_2^{20} \frac{f_c mc_i}{2D_d^3} \left[1 + erf\left(\frac{\ln(2/\bar{D_s})}{\sqrt{2}\ln(\sigma_s)}\right)\right] \exp\left[-\left(\frac{D_d}{\lambda}\right)^3\right] dD_d$$
$$+ \sum_{i=4}^{8} \int_0^{20} \frac{f_c mc_i + f_s ms_i}{2D_d^3} \left[1 + erf\left(\frac{\ln(D_d/\bar{D_s})}{\sqrt{2}\ln(\sigma_s)}\right)\right] \exp\left[-\left(\frac{D_d}{\lambda}\right)^3\right] dD_d \quad (64)$$

$$C_V = \sum_{i=1}^{3} \int_0^2 \frac{f_c mc_i}{2} \left[1 + erf\left(\frac{\ln(D_d/\bar{D_s})}{\sqrt{2}\ln(\sigma_s)}\right)\right] \exp\left[-\left(\frac{D_d}{\lambda}\right)^3\right] dD_d$$
$$+ \sum_{i=1}^{3} \int_2^{20} \frac{f_c mc_i}{2} \left[1 + erf\left(\frac{\ln(2/\bar{D_s})}{\sqrt{2}\ln(\sigma_s)}\right)\right] \exp\left[-\left(\frac{D_d}{\lambda}\right)^3\right] dD_d$$
$$+ \sum_{i=4}^{8} \int_0^{20} \frac{f_c mc_i + f_s ms_i}{2} \left[1 + erf\left(\frac{\ln(D_d/\bar{D_s})}{\sqrt{2}\ln(\sigma_s)}\right)\right] \exp\left[-\left(\frac{D_d}{\lambda}\right)^3\right] dD_d \quad (65)$$

5.4 Whether or not the theory and mathematical algorithms were peer reviewed, and if so, include summary of theoretical strengths and weaknesses

The semi-empirical approach has been peer reviewed and is available in Perwitz et al. (2015a). The theoretical approach is not peer reviewed as of today. A publication is in preparation. Strengths and weaknesses have been highlighted throughout the report and are detailed in Perlwitz et al. (2015a)

5.5 Hardware requirements and documentation

ModelE code, documentation and hardware requirements can be found here:
http://www.giss.nasa.gov/tools/modelE/

It's all public, including the option in the code for the minerals.

Specific documentation on the semi-empirical approach for minerals can be found in Perlwitz et al. (2015a).

Specific peer reviewed documentation for the theoretical approach is under preparation.

6 References

Cakmur, R. V., Miller, R. L., and Torres, O. 2004: Incorporating the effect of small-scale circulations upon dust emission in an atmospheric general circulation model, J. Geophys. Res., 109, D07201.

Claquin, T., Schulz, M., and Balkanski, Y. J. 1999: Modeling the mineralogy of atmospheric dust sources, J. Geophys. Res., 104, 22,243?22,256.

d'Almeida GA, Schtz L 1983: Number, mass and volume distributions of mineral aerosol and soils of the Sahara. J Clim Appl Meteorol, 22:233-243.

Kandler, K., Schutz, L., Deutscher, C., Ebert, M., Hofmann, H., Jackel, S., Jaenicke, R., Knippertz, P., Lieke, K., Massling, A., Petzold, A., Schladitz, A., Weinzierl, B., Wiedensohler, A., Zorn, S., and Weinbruch, S. 2009: Size distribution, mass concentration, chemical and mineralogical composition and derived optical parameters of the boundary layer aerosol at Tinfou, Morocco, during SAMUM 2006, Tellus B, 61, 32?50.

FAO: Digital Soil Map of the World, Food and Agriculture Organization, Rome, Italy, 2007.

FAO/IIASA/ISRIC/ISSCAS/JRC: Harmonized World Soil Database (version 1.2), FAO, Rome, Italy and IIASA, Laxenburg, Austria.

Ginoux, P., Chin, M., Tegen, I., Prospero, J. M., Holben, B., Dubovik, O., and Lin, S.-J. 2001: Sources and distributions of dust aerosols simulated with the GOCART model, J. Geophys. Res., 106, 20,255?20,273.

Goldstein H, et al. 2005: Particle-size, CaCO3, chemical, magnetic, and age data from surficial deposits in and around Canyonlands National Park, Utah. US Geological Survey.

Ito, A. and Xu, L. 2014: Response of acid mobilization of iron-containing mineral dust to improvement of air quality projected in the future, Atmos. Chem. Phys., 14, 3441-3459.

Koch, D., Jacob, D., Tegen, I., Rind, D., and Chin, M. 1999: Tropospheric sulfur simulation and sulfate direct radiative forcing in the Goddard Institute for Space Studies general circulation model, 30 J. Geophys. Res., 104, 23,799-23,822.

Kok, J. F. 2011: A scaling theory for the size distribution of emitted dust aerosols suggests climate models underestimate the size of the global dust cycle, PNAS, 108, 1016-1021

Miller, R. L., Cakmur, R. V., Perlwitz, J., Geogdzhayev, I. V., Ginoux, P., Koch, D., Kohfeld, K. E., Prigent, C., Ruedy, R., Schmidt, G. A., and Tegen, I. 2006: Mineral dust aerosols in the NASA Goddard 30 Institute for Space Sciences ModelE atmospheric general circulation model, J. Geophys. Res., 111, D06208.

Perlwitz, J.P., C. Perez Garcia-Pando, and R.L. Miller, 2015a: Predicting the mineral composition of dust aerosols - Part 1: Representing key processes. Atmos. Chem. Phys., 15, 11593-11627.

Perlwitz, J.P., C. Perez Garcia-Pando, and R.L. Miller, 2015b: Predicting the mineral composition of dust aerosols - Part 2: Model evaluation and identification of key processes with observations. Atmos. Chem. Phys., 15, 11629-11652.

Shao, Y., Raupach, M. R., and Leys, J. F. 1996: A model for predicting aeolian sand drift and dust entrainment on scales from paddock to region, Aust. J. Soil Res., 34, 309-342.

Scheuvens, D., Schutz, L., Kandler, K., Ebert, M., and Weinbruch, S. 2013: Bulk composition of northern African dust and its source sediments and its source sediments - A compilation, Earth-Science Reviews, 116, 170-194.

Scheuvens, D. and Kandler, K. 2014: On Composition, Morphology, and Size Distribution of Airborne Mineral Dust, in: Mineral Dust: A Key Player in the Earth System, edited by Knippertz, P. and Stuut, J.-B., chap. 2, pp. 15?49, Springer Netherlands, Dordrecht, Heidelberg, New York, London.

Schmidt, G. A., Kelley, M., Nazarenko, L., Ruedy, R., Russell, G. L., Aleinov, I., Bauer, M., Bauer, S. E., Bhat, M. K., Bleck, R., Canuto, V., Chen, Y.-H., Cheng, Y., Clune, T. L., Del Genio, A., de Fainchtein, R., Faluvegi, G., Hansen, J. E., Healy, R. J., Kiang, N. Y., Koch, D., Lacis, A. A., LeGrande, A. N., Lerner, J., Lo, K. K., Matthews, E. E., Menon, S., Miller, R. L., Oinas, V., Oloso, A. O., Perlwitz, J. P., Puma, M. J., Putman, W. M., Rind, D., Romanou, A., Sato, M., Shindell, D. T., Sun, S., Syed, R. A., Tausnev, N., Tsigaridis, K., Unger, N., Voulgarakis, A., Yao, M.-S., and Zhang, J. 2014: Configuration and assessment of the GISS ModelE2 contributions to the CMIP5 archive, J. Adv. Model. Earth Sys., 6, 141-184.

Shi, Z., Bonneville, S., Krom, M. D., Carslaw, K. S., Jickells, T. D., Baker, A. R., and Benning, L. G. 2011: Iron dissolution kinetics of mineral dust at low pH during simulated atmospheric processing, Atmos. Chem. Phys., 11, 995-1007.

Wesely, M. L. and Hicks, B. B. 1977: Some factors that affect the deposition rates of sulfur dioxide and similar gases on vegetation, J. Air Pollut. Control Assoc., 27, 1110-1116.